

## Statistical patterns of high-latitude convection obtained from Goose Bay HF radar observations

J. M. Ruohoniemi and R. A. Greenwald

Applied Physics Laboratory, Johns Hopkins University, Laurel, Maryland

**Abstract.** We have derived patterns that describe the statistical interplanetary magnetic field (IMF) dependencies of ionospheric convection in the high-latitude region of the northern hemisphere. The observations of plasma motion were made with the HF coherent backscatter radar located at Goose Bay, Labrador, over the period September 1987 to June 1993. The area covered by the measurements extended poleward of  $65^\circ\Lambda$  to a working limit of about  $85^\circ\Lambda$ . Distributions of electrostatic potential have been derived and expressed as series expansions in spherical harmonics. The patterns are the first derived from direct ground-based observations of ionospheric convection that approach in completeness and level of detail the patterns derived in recent satellite studies [Rich and Hairston, 1994; Weimer, 1995]. We show the dependence of the convection on IMF angle in the GSM  $y$ - $z$  plane for three intervals of IMF magnitude in this plane. Except for predominantly northward IMF, the convection is primarily two-cell. The dusk cell is larger in terms of both spatial extent and potential variation. The effect of IMF  $B_y$  is apparent in the global shaping of the cells and the orientation of the overall pattern in MLT; for  $B_y+$  ( $B_y-$ ) the dusk (dawn) cell is more round (crescent-shaped) and the pattern more rotated toward earlier MLTs. The  $B_y$  effect on the nightside convection is pronounced and is hemispherically antisymmetric, like the well-known dayside  $B_y$  effect. For IMF increasingly northward, the convection trajectories on the dayside become increasingly distorted, evolving through a three-cell to a four-cell circulation. The additional cells appear on either side of the noon meridian and result in sunward flow. The overall agreement with the results of the satellite studies is good and extends to quite fine detail in the case of the comparison with Weimer [1995]. There are significant differences with the statistical patterns derived from magnetometer measurements, which tend to show domination by the dawn rather than the dusk cell.

### 1. Introduction

The plasma of the high-latitude magnetosphere is maintained in a nearly continuous state of motion by the transfer of energy and momentum from the solar wind. The characteristics of the plasma convection are especially influenced by the interplanetary magnetic field (IMF) carried by the solar wind plasma [e.g., Heelis, 1984; Heppner and Maynard, 1987]. Important aspects of the solar wind-magnetosphere interaction can be studied on the basis of statistical models of the convection. Convection maps provide valuable inputs for the modeling of magnetospheric processes such as the transport of ionization through the high-latitude regions and the transfer of energy to the neutral atmosphere.

Recently, detailed models of high-latitude convection have been derived by statistical analysis of data collected by polar orbiting satellites [Rich and Hairston, 1994; Weimer, 1995]. These show the tendency of convection to be organized by IMF orientation and magnitude and the influence of such factors as season and dipole tilt. The detailed elucidation of these effects was possible because the satellites have accumulated very large sets of convection velocity measurements.

Ground-based studies have also shown general associations of convection with factors such as IMF orientation and geo-

magnetic activity level [e.g., Friis-Christensen *et al.*, 1985; Holt *et al.*, 1987]. Recent work has considered seasonal factors [de la Beaujardière *et al.*, 1991] and combined seasonal/ $B_y$  effects [Ruohoniemi and Greenwald, 1995]. An extensive convection model has been derived from magnetic disturbance data collected with magnetometers [Papitashvili *et al.*, 1994]. Studies that utilize the more direct radar observations of convection velocity have not reached the levels of coverage and detail of the recent satellite studies.

In this paper we report on the characteristics of high-latitude convection as determined from a statistical analysis of measurements made with a ground-based coherent HF radar. The results are presented in the form of maps parameterized mainly by IMF. The maps show the modulation of the basic two-cell morphology by the IMF  $B_y$  component and the emergence of multicell convection for dominant  $B_z+$ . We discuss the IMF dependencies and compare with previous work. Our set of convection patterns constitute an independent model for application to various problems in magnetospheric physics.

In the next section we discuss the data set and the methods of deriving statistical maps of the convection velocity and electrostatic potential distribution. Since the coverage afforded by the radar is incomplete (e.g., does not extend through the highest latitudes in the polar cap), we apply Laplace's condition to extend the mapping through the entire high-latitude region. The global electrostatic potential distribution is finally expressed as a series expansion in spherical harmonics. We present the patterns obtained for representative combinations of IMF orientation and magnitude.

Copyright 1996 by the American Geophysical Union.

Paper number 96JA01584.  
0148-0227/96/96JA-01584\$09.00

In a statistical study of this sort, it is customary to perform tests of significance on the results. For example, one may consider the variance in the measurements. In this presentation we shall not take this approach. In our view, the tests of significance that can be performed within the context of measurements obtained by a single technique are less convincing than those that cross disciplinary boundaries. Thus we shall only briefly discuss the statistical limits of the radar data set, preferring instead to let comparisons with the findings of *Rich and Hairston* [1994] and *Weimer* [1995] demonstrate the range of validity.

## 2. Data Processing

The measurements of convection velocity were made with the Johns Hopkins University Applied Physics Laboratory HF radar located at Goose Bay, Labrador (53.4°N, 60.4°W). This instrument has operated nearly continuously since 1985. The technical aspects of its operation were described by *Greenwald et al.* [1985]; here we discuss those details of particular relevance to the current study.

In its usual operating mode the radar scans over a 52° azimuth sector centered on 5° east of geographic north in 16 discrete steps with a scan repeat time of 100 s. The backscatter returns are range-gated in steps of 30 or 45 km. The outer range limit for sampling is typically 2500 km. For this study the processing is limited to data returned from ranges greater than 600 km. The effective coverage then extends poleward of 65°A to about 85°A.

The operating frequency lies in the 10–18 MHz interval. Backscattering can occur if decameter-scale field-aligned ionization irregularities are present in the ionosphere. Such irregularities are a common feature of the high-latitude regions [*Baker et al.*, 1988; *Leonard*, 1991]. At *F* region altitudes their motion is equal to that of the ambient plasma [*Villain et al.*, 1985; *Ruohoniemi et al.*, 1987]. Backscatter is generated from HF rays that encounter irregularities while propagating orthogonally to the geomagnetic field lines. A radar measurement of the drift of the irregularities thus provides an estimate of the line-of-sight component of the cross field or  $\mathbf{E} \times \mathbf{B}$  (convection) velocity.

We have processed the convection velocity data collected with the Goose Bay radar over the period September 1987 to

July 1993 into a format that is more suited for statistical analysis. This consisted of averaging the velocity measurements within 12-min UT intervals and spatial bins measuring  $1^\circ \times 3^\circ$  in latitude/longitude coordinates. (We use the magnetic coordinate system of *Baker and Wing* [1989].) The result is effectively a time series of the line-of-sight velocity measured over the radar field of view for the entire ~6-year period. This file can be sorted according to any selection of values for the indices (e.g., *Kp*, IMF) contained in a parallel "indicial" database. Sorting produces a 24-hour synoptic file of the average line-of-sight velocity at 12-min UT steps for the stated conditions.

The synoptic file is converted into a global map of the two-dimensional plasma motion by the process of "time-tagging." That is, the MLT of each line-of-sight velocity value is determined from its magnetic longitude and UT. As the UT varies, a cell of the convection pattern tagged by fixed values of MLT and  $\Lambda$  is successively observed from different directions. The velocity vector is determined by fitting the angular variation of the line-of-sight velocity in the cell. An example is shown in Figure 1. A cell can typically be tracked through 2–3 hours of UT. This method is inappropriate for mapping real-time convection since stationarity will not usually be obtained for such extended periods. In a statistical study, however, one extracts a set of measurements that is characteristic of a particular state of the global convection and can obtain a fairly rigorous solution of the vectorization problem. Additional details of the conversion of the velocity data to convection maps can be found in the work by *Ruohoniemi and Greenwald* [1995].

Examples of vector velocity maps are shown in Figure 2. The data have been sorted for a moderate level of geomagnetic disturbance ( $2- \leq Kp \leq 3+$ ) and dominance by IMF  $B_y$  ( $|B_y| > |B_z|$ ). For clarity, the vectors have been averaged in 1-hour MLT intervals. The two maps show the general  $B_y$ -sign dependencies of the convection pattern. In particular, the flow in the vicinity of the noon meridian for the  $B_y-$  case rotates to duskward with increasing latitude in the 70°–85°A range while for  $B_y+$  this flow is more zonal and directed downward. It is also apparent that latitudinal velocity shear is concentrated in the dusk sector for  $B_y-$  and in the dawn sector for  $B_y+$ . Two dropouts in the coverage above 65°A are apparent, namely, the high polar cap and the lower latitude region on the dayside. In these areas the number of echoes received were deemed insufficient to justify the estimation of velocity vectors. As dis-

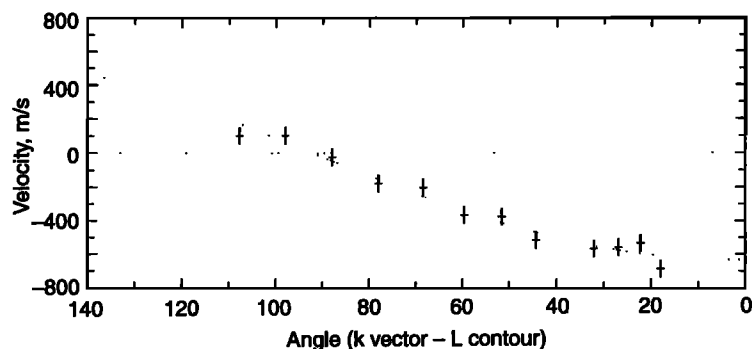


**Figure 1.** An example of the estimation of a convection velocity vector by the method of time tagging (see text). The velocity data have been sorted as per the discussion of Figure 2, the case of  $B_y > 0$ . The convection cell indexed by the coordinates (1806 MLT, 71.5°A) enters the radar field of view near 1930 UT and exits near 2200 UT. The average line-of-sight velocity is plotted as a function of the angle at the cell between the radar look direction and the invariant latitude contour. The sinusoidal fitting indicates a westward drift of 630 m/s and an equatorward drift of 24 m/s. (Error bars are for illustrative purposes only.)

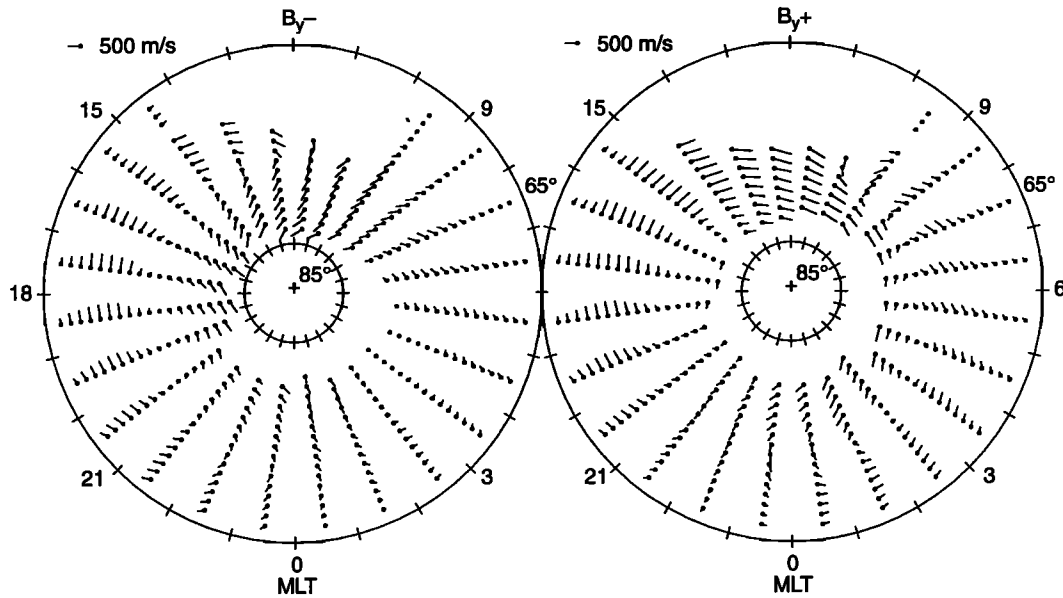


**Figure 2.** Maps of the average convection velocity obtained for conditions of  $2- \leq Kp \leq 3+$ ,  $|B_y| > |B_z|$ , and (left)  $B_y < 0$  and (right)  $B_y > 0$ . The outer and inner circles correspond to  $65^\circ$  and  $85^\circ\Lambda$ , respectively. The lowest latitude for which vectors are shown is  $66.5^\circ\Lambda$  and the step in latitude is  $1^\circ$ .

cussed earlier, the effective upper latitude limit for sampling is about  $85^\circ\Lambda$ . In addition, the number of echoes received decreases with latitude before this limit because of the radar viewing geometry (fewer beams sample at such high latitudes) and the expected decrease in backscattered power with range from the radar. On the dayside relatively few echoes are received below the latitude of the cusp/cleft region, owing partly to the absence of irregularities and partly to propagation factors, particularly a preponderance of backscatter from the Earth's surface ("ground-scatter"). A discussion of the factors that condition the scatter occurrence rate appears elsewhere (J. M. Ruohoniemi, "Rates of scattering occurrence in routine HF radar observations," manuscript in preparation, 1996). The region below  $65^\circ\Lambda$  is also effectively a coverage dropout. In the following we shall analyze these velocity maps for "best fit" estimates of the global convection pattern.

It is well known that the onset of a change in the magnetospheric convection that is due to an IMF variation lags the arrival of the solar wind at the magnetopause by a time delay that varies with MLT [e.g., *Bargatze et al.*, 1985]. At noon the delay can be as little as a few minutes [*Greenwald et al.*, 1990; *Ruohoniemi et al.*, 1993], while on the nightside it may approach 1 hour [*Lockwood et al.*, 1990]. The response of the magnetosphere might not be a simple function of MLT, however; *Knipp et al.* [1993] reported that the convection responds more rapidly to some types of IMF turnings than to others. In addition, the state of the convection at a given instant may reflect the time history of the IMF. In this study we allow for the time factors in an approximate fashion. The IMF data are first averaged within the 12-min UT intervals that are used to reduce the radar data. When the radar data are sorted by IMF, a given UT bin is tagged with the average of the IMF over a time interval that varies with the MLT of the bin. On the dayside (8–16 MLT) a 12-min UT data bin is flagged with the average of the IMF over the concurrent and previous 12-min UT intervals. On the flanks (4–8 MLT and 16–20 MLT) IMF is averaged over the concurrent and two earlier UT intervals while on the nightside (20–4 MLT) the concurrent and three earlier

UT intervals are used. The sampling interval for IMF sorting thus progresses from 24 to 48 min from the dayside to the nightside. As noted by *Rich and Hairston* [1994], the IMF on timescales of tens of minutes is more often steady than time-varying. We have found that varying the delay factors by reasonable amounts makes only slight differences to the resulting patterns.

In this paper we focus on the basic IMF dependencies of the convection. Other factors, such as the solar wind velocity [*Papitashvili et al.*, 1994], season [*Rich and Hairston*, 1994], dipole tilt [*Weimer*, 1995], disturbance level [*Senior et al.*, 1990], and substorm phase [*Shue and Weimer*, 1994] are acknowledged but not treated in detail. This is partly a statistical limitation. Given that the primary sorting is IMF, any secondary sorting greatly diminishes the number of counts contributing to the bin-averages and the resulting patterns are less well determined than those sorted only by IMF. In sufficiently constrained circumstances, of course, it is simply not possible to generate a reliable pattern. Analysis of secondary factors may require analyses more limited in scope or considerably modified from that presented here. (An example is the analysis of simultaneous  $B_y$  and seasonal effects in nightside convection described by *Ruohoniemi and Greenwald* [1995].)

With respect to the seasonal factor, we note that the contributions to the overall statistics were greatest for winter and least for summer. This was due in part to more frequent interruption of the radar operation in summer and in part to a winter-to-summer decrease in the overall rate of scattering occurrence. The convection patterns that we describe here can hence be expected to have somewhat more winter-equinoctial character.

### 3. Conversion to Global Maps of Equipotential Contours

#### 3.1. Procedure

The convection electric field  $\mathbf{E}$  is related to the distribution of electrostatic potential,  $\Phi$ , through the expression:

$$\mathbf{E} = -\nabla\Phi \quad (1)$$

It is convenient to express the potential in terms of an expansion in basis functions. Various expansions are possible, for example, *Weimer* [1995] utilized the associated spherical harmonics while *Alcaydé et al.* [1986] and *Senior et al.* [1990] worked in Legendre polynomials. An expansion in spherical harmonics is most suitable when the area of observations includes the high polar cap. At the last stage of our analysis we obtain expressions for the global distribution of the potential in terms of spherical harmonics. Here we describe the manner in which the radar velocity data are converted into maps of the global convection pattern.

1. The starting point is a map of velocity vectors such as those shown in Figure 2. The radar coverage corresponds approximately to an annular ring bounded by the  $65^\circ\Lambda$  and  $85^\circ\Lambda$  contours. This geometry suggests the formulation of *Alcaydé et al.* [1986] and *Senior et al.* [1990], who expressed the potential in terms of a polynomial expansion in latitude and a Fourier expansion in MLT:

$$\Phi(x, \phi) = -\sum_{n=0}^N \sum_{m=0}^M \phi_{nm} P_n(x) e^{im\phi} \quad (2)$$

where the  $\phi_{nm}$  are complex coefficients and the  $P_n(x)$  are the classical Legendre polynomials, with

$$\begin{aligned} x &= (2\Lambda - \Lambda_m)/\Delta\Lambda \\ \Delta\Lambda &= \Lambda_{\min} - \Lambda_{\max} \\ \Lambda_{\min} &= \Lambda_{\max} + \Lambda_{\min} \end{aligned} \quad (3)$$

and  $\Lambda_{\min}$  and  $\Lambda_{\max}$  are the lower and upper latitude limits for sampling,  $65^\circ\Lambda$  and  $85^\circ\Lambda$ , respectively. The vector velocity data provide the set of electric field estimates through the relation  $\mathbf{E} = -\mathbf{v} \times \mathbf{B}$  that can be used to solve for the coefficients. The quantity minimized is

$$D = \sum_i |\mathbf{E}_i - \nabla\Phi|^2 \quad (4)$$

The values of  $N$  and  $M$  determine the smallest spatial structures that can be resolved. For the results presented here  $N=6$  and  $M=6$ , corresponding to limiting resolutions of  $3.3^\circ$  in latitude and 4 hours in MLT. The minimization is carried out by a numerical procedure. The main characteristics of the potential distribution are found to be expressed by the coefficients of lower degree ( $N, M < 5$ ).

Figure 3 shows the maps of the electric potential distribution derived from the convection data of Figure 2. Contours are drawn only where the fitting was constrained by velocity data. A pattern dominated by two circulation cells is obtained. The dusk cell is clearly more crescent-shaped for  $B_y^-$  and more round for  $B_y^+$ ; the  $B_y$  dependence of the dawn cell is the reverse. The crescent-shaped cell dominates the flows in the vicinity of the midnight MLT meridian. The line joining the cell centers is nearly aligned with the dusk-dawn meridian for  $B_y^-$  but is rotated toward earlier hours for  $B_y^+$ .

In these plots the potential variations are significant; however, the convection generally extends equatorward of the  $65^\circ\Lambda$  limit of the observations and it is not possible to unambiguously establish a zero potential reference. The potential is uncertain by an additive constant. In this analysis we have adopted the following convention: the potential is set so that its average on the nightside (18–06 MLT) at the low-latitude limit ( $65^\circ\Lambda$ ) of the observations is zero. While not ideal, this convention is objective and usually identifies the zero potential condition with a contour that exits the nightside polar cap close to the 0 MLT meridian. The total potential variation for the cases shown here is about the same ( $\sim 50$  kV) and more of the variation appears across the dusk cell.

2. It is desirable to have the convection mapped over the entire high-latitude zone, that is, through the polar cap and to the low-latitude limit of convection where direct radar measurements of the convection are lacking. Naively, one might suppose that the expansion of (2) with the coefficients obtained in

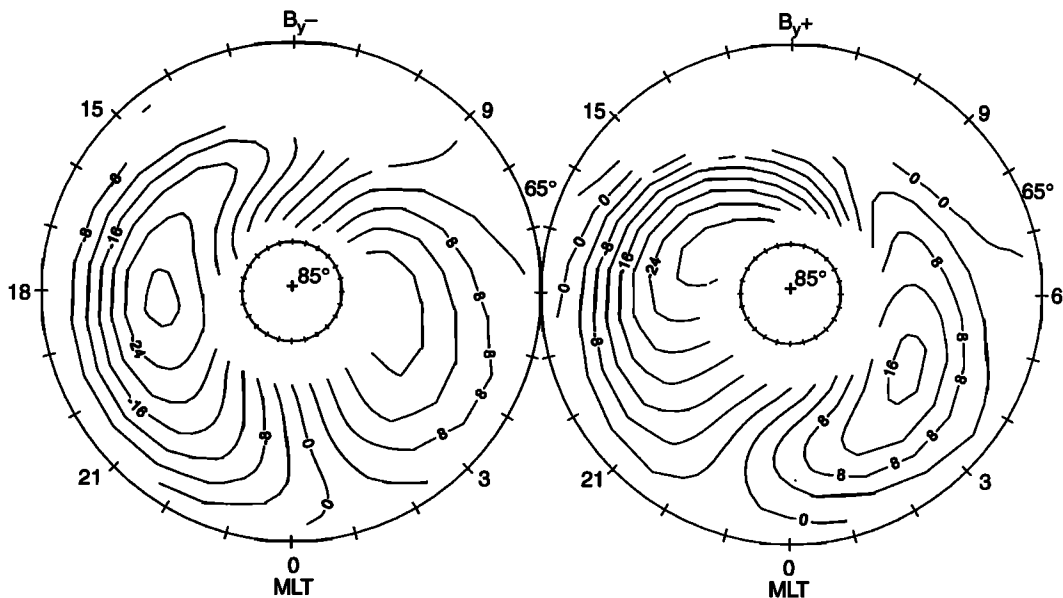


Figure 3. Electrostatic equipotential representations of the velocity maps shown in Figure 1. The zero potential contour is set as explained in the text.

step 1 could be applied in these regions. However, the results are not satisfactory, as the fitting procedure produces an optimal match between the coefficients and the measurements and there are no constraints on the solution in the regions without measurements. For example, one expects that for sufficiently low latitude the potential would approach zero but this information is not embedded in the numerical solution of (2).

Alternatively, one could complete the contours by means of a free-hand drawing. A process of manual smoothing was performed by *Rich and Hairston* [1994] to reduce global distributions of electrostatic potential values to contours. The patterns of Figure 3 do appear to be sufficiently complete to justify such an exercise. Two drawbacks to this approach are the obvious subjectivity of the mapping and the lack of a digital representation of the result.

We prefer a mathematical method of completing the maps that is based on satisfying Laplace's equation in the regions of no radar velocity data. That is, we extrapolate the mapping of the contours into the regions above and below the latitudinal limits of the velocity coverage by applying the condition

$$\nabla^2 \Phi = 0 \quad (5)$$

Laplace's condition is satisfied in a region of no field-aligned current, vertical magnetic field, and spatially uniform height-integrated conductivity [*Freeman and Southwood*, 1988]. As partial justification, we note that the statistical distributions of *Iijima and Potemra* [1978] show the high polar cap and low-latitude regions, where the bulk of the pattern extrapolation must be performed, as comparatively free of field-aligned current. (This will be less true of the polar cap under strongly northward IMF conditions due to the addition of the NBZ current system described by *Iijima et al.* [1984].) *Foster et al.* [1986a] applied Laplace's condition to extend their mapping of equipotential contours to the region above 75°A. Here we use it similarly to provide an initial global solution; at the final stage of processing the condition will be partially relaxed.

Laplace's equation on a spherical surface of fixed radius  $R$  reduces to

$$\frac{1}{R^2 \sin \theta} \frac{\partial}{\partial \theta} \left( \sin \theta \frac{\partial \Phi}{\partial \theta} \right) + \frac{1}{R^2 \sin^2 \theta} \frac{\partial^2 \Phi}{\partial \phi^2} = 0 \quad (6)$$

A suitable solution for this problem was formulated by *Freeman et al.* [1991]. They defined a modified polar angle:

$$x = \ln \{ \tan(\theta/2) \} \quad (7)$$

and obtained

$$\Phi(x, \phi) = \sum_{m=0}^{\infty} \{ a_m e^{mx} \sin(m\phi) + b_m e^{-mx} \sin(m\phi) + c_m e^{mx} \cos(m\phi) + d_m e^{-mx} \cos(m\phi) \} \quad (8)$$

The coefficients are determined by stating the boundary conditions. In each of the maps of Figure 3, we identify a high-latitude "boundary" with the set of points lying at the highest latitude in each MLT interval for which potential values constrained by velocity estimates are available. We similarly define a low-latitude boundary. We further require that below the low-latitude boundary the potential reduce to zero by some reference latitude  $\Lambda_0$ . In the regions beyond the boundaries (8) assumes simpler forms. (The reader is referred to the appendix of *Freeman et al.* [1991] for details.) The coefficients of the expansion for  $\Phi$  in either region are found by matching in a best fit sense the appropriate expression of (8) with the distribution of the potential around the associated boundary.

Figure 4 shows the maps of extrapolated equipotential contours obtained for the examples of Figure 3 with  $\Lambda_0 = 60^\circ$ . (The maps have been rescaled to show a lowest latitude of  $50^\circ$ .) The equipotential contours in the area of velocity coverage are unchanged. In the high-latitude region the contours are very simply connected across the dawn-dusk meridian. In the low-latitude region the contours primarily close within either the dusk or dawn sector and finish at the reference latitude contour. The designation of potential by the convention described earlier seems reasonable in the sense that the contours crossing the noon-midnight meridian into the dawn or dusk sector do not

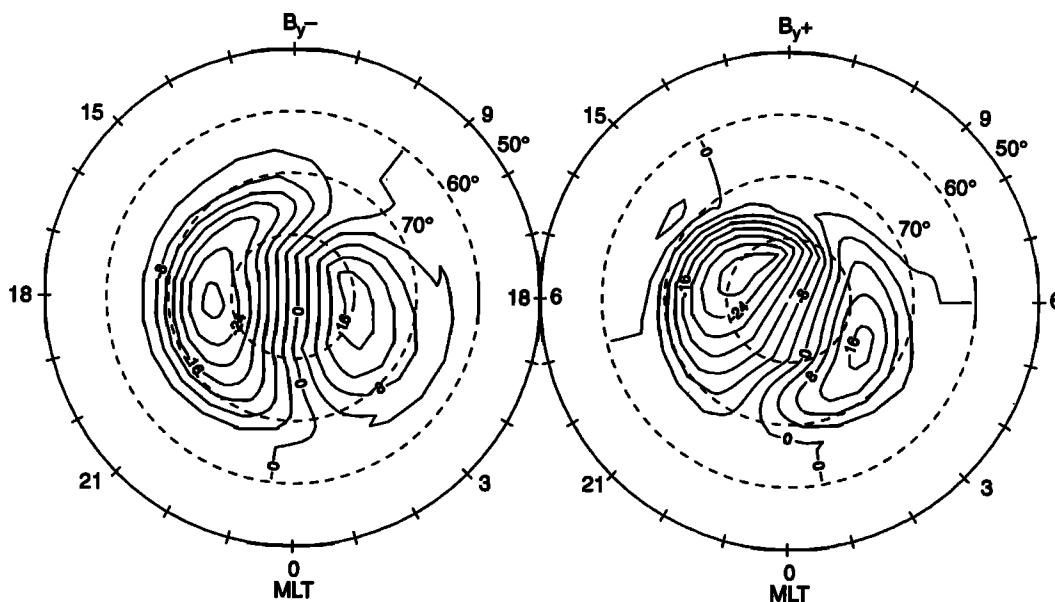
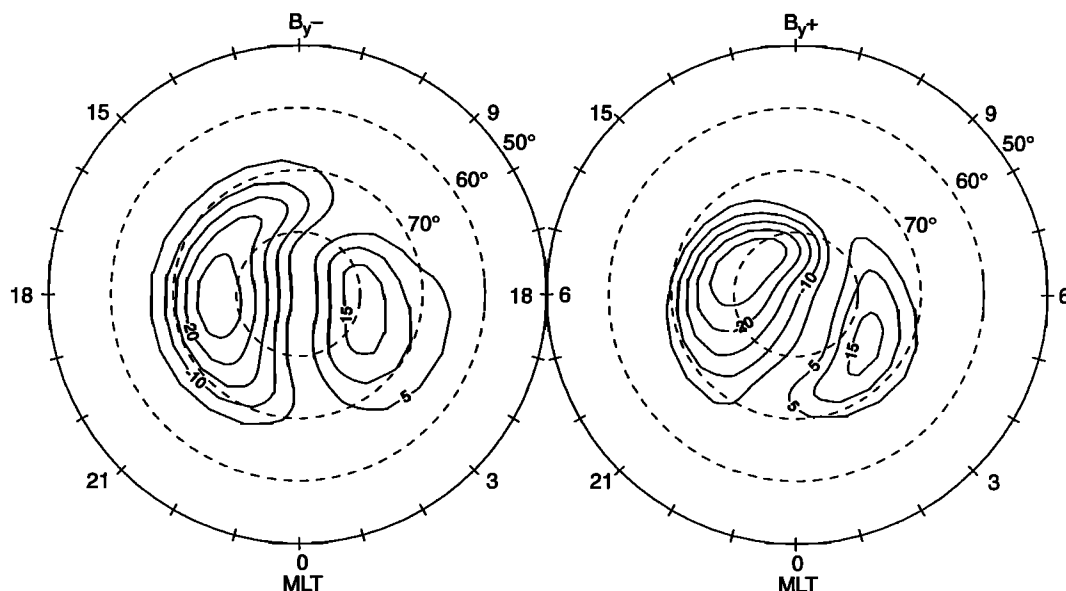


Figure 4. Extrapolation of the equipotential representations of Figure 3 via application of Laplace's condition. The potential has been set to zero at a latitude of  $60^\circ$ A. The outer circle is drawn for a latitude of  $50^\circ$ A.



**Figure 5.** Final equipotential representations of the global convection obtained by expressing the potential distribution of Figure 4 in terms of spherical harmonics as described in the text. The contour step is 5 kV. For clarity, the zero-potential contour is not shown.

execute long excursions before reversing direction and ultimately closing in the sector of origin. Limitations in the numerical fitting of the potential described above are apparent as slight discontinuities in the equipotential contours at the low-latitude boundary, and the abrupt turnings of the contours at the high-latitude boundary are clearly an artifact. With these qualifications, we obtain a rudimentary solution of the global mapping problem. The principal characteristics of the patterns, such as the positions of the cell centers and the potential variation, are set by the radar velocity observations in the intermediate-latitude region.

3. As the final step, we express the potential patterns as series expansions in spherical harmonic functions. This renders compact representations with desired properties of continuity and differentiability. We can also take advantage of the filtering implicit in such a decomposition to relax Laplace's condition in the high- and low-latitude regions.

The potential function over the surface of a sphere can be expanded in spherical harmonics as described by *Jackson* [1962] and *Weimer* [1995]:

$$\Phi(\theta, \phi) = \sum_{l=0}^{\infty} \sum_{-l}^l A_{lm} Y_{lm}(\theta, \phi) \quad (9)$$

where the spherical harmonic functions are

$$Y_{lm}(\theta, \phi) = \sqrt{\frac{2l+1}{4\pi} \frac{(l-m)!}{(l+m)!}} P_l^m(\cos\theta) e^{im\phi} \quad (10)$$

and the coefficients are

$$A_{lm} = \int d\Omega Y_{lm}^*(\theta, \phi) \Phi(\theta, \phi) \quad (11)$$

In this problem the potential is specified over the portion of the sphere that lies above a zero-potential reference latitude,  $\Lambda_0$ . Equations (9) and (10) can be solved if the colatitude is replaced with an "effective" colatitude defined by

$$\theta' = \frac{\pi}{\left(\frac{\pi}{2} - \Lambda_0\right)} \theta \quad (12)$$

Limiting the expansion to finite order in  $l$  and  $m$  amounts to low-pass filtering. The basic features of the patterns are found in the lower orders. The results presented here were obtained with  $l, m \leq 6$ .

Figure 5 shows the results of subjecting the potential distributions of Figure 4 to a decomposition in spherical harmonics. The patterns portray realistic convection trajectories over the entire high-latitude zone. Comparison with Figure 3 shows that the main characteristics of the potential distribution in the areas of direct velocity measurement are preserved. In the high- and low-latitude regions of no direct velocity measurement the filtering implicit in the spherical harmonic analysis relaxes Laplace's condition. (The details of the potential distributions in these regions must of course be considered less well determined.) Maps of the type shown in Figure 5 along with the spherical harmonic representations of the potential patterns (i.e., the  $A_{lm}$  coefficients of (8)) are the final product of this analysis.

The convection maps of Figure 5 indicate that the influence of  $B_y$  is felt primarily through a global round/crescent shaping of the cells and a rotation of the overall pattern in MLT. The dusk cell is spatially larger and carries more potential variation for both signs of  $B_y$ , and the total potential drops are the same ( $\sim 50$  kV). For  $B_{y-}$  the dusk cell is more crescent-shaped and the dawn cell more round; the polarity of the shaping is the reverse for  $B_{y+}$ . With reference to the "axes" defined by the line joining the cell centers and the direction of flow in the high polar cap, the pattern is nearly aligned with the dawn-dusk and noon-midnight meridians for  $B_{y-}$  but rotates substantially ( $\sim 2$  hours) to earlier MLTs for  $B_{y+}$ . The dusk cell dominates the noon meridian at auroral latitudes in both cases; however, the crescent-shaped cell as selected by the sign of  $B_y$  dominates the midnight meridian. The  $B_y$  dependence on the noon meridian is seen primarily in the structuring of the flows in the dusk cell. Although the impact of IMF  $B_y$  variations is undoubtedly more

immediate and direct on the dayside, this comparison indicates that the nightside also responds.

Another  $B_y$  factor that can be discerned in Figure 5 is a shift of the overall pattern toward the dawnside for  $B_{y+}$  compared to  $B_{y-}$ . The displacement of the cell centers measures several degrees in invariant latitude. This shift is consistent with that described for the auroral oval [Holzworth and Meng, 1984] and has been interpreted by Cowley *et al.* [1991] in terms of a partial penetration of the IMF into the magnetospheric cavity.

The Harang discontinuity is a feature often discussed in relation to nightside convection [e.g., Heppner and Maynard, 1987]; it is defined as the locus of points at which the zonal velocity reverses from westward to eastward with increasing latitude and is generally understood to slant equatorward with increasing MLT in the evening sector. In Figure 5 a Harang discontinuity can be clearly identified only in the  $B_{y-}$  case where it coincides with the axis (i.e., line of maximum latitudinal velocity shear) of the crescent-shaped dusk cell. For this sign of  $B_y$ , the rounded dawn cell contributes equatorward flow in the postmidnight period. In the  $B_{y+}$  case the rounded dusk cell contributes equatorward convection in the premidnight period and a prominent latitudinal velocity reversal is found in the postmidnight period along the axis of the crescent-shaped dawn cell. Thus the nightside convection is ordered by the sign of  $B_y$  into sectors of more equatorward and more latitudinally sheared flow. The sense of the ordering described here, with the velocity shear associated with the dusk (dawn) cell for  $B_{y-}$  ( $B_{y+}$ ) is the opposite of that reported in the southern hemisphere by Leonard *et al.* [1995], demonstrating that the well-known hemispheric antisymmetry of the  $B_y$  effect on the dayside convection extends to the nightside.

### 3.2. Uncertainties

The uncertainties encountered in the course of converting the radar velocity data to global convection maps derive chiefly from the limited coverage of the convection region provided by the radar. First, as we have discussed, the unambiguous designation of a zero-potential contour is generally not possible; we have adopted a convention which, while appearing to give reasonable results, leaves somewhat uncertain the exact division of the total potential variation between the convection cells. Second, we designate a low-latitude limit to the convection. In reality this limit is not truly fixed in invariant coordinates because the convection electric fields can penetrate to midlatitudes [Wand and Evans, 1981]. While the selection of a particular limit for a certain level of geomagnetic disturbance can be justified, the details of the convection in the low-latitude region are subject to uncertainty from the ambiguity in this designation. For the patterns presented here we have applied  $\Lambda_0 = 60^\circ$  except where otherwise indicated. The equipotential contours are also extrapolated into the high polar cap. It is preferable that as large an area as possible be mapped by radar velocity data so that the constraints imposed by actual measurements fix the pattern in the unmapped regions. In the following we have selected binning intervals in  $Kp$  and IMF that provide radar velocity coverage comparable to that of Figures 2 and 3. By varying the selection criteria we have verified that the resulting patterns are solved to a high degree of confidence, that is, the important features of the pattern are stable against moderate variation of the selection criteria.

It has become common practice to present statistical convection maps in the form of clockdial plots with the plot position varying with the angle of the IMF vector in the GSM  $y$ - $z$  plane [e.g., Rich and Hairston, 1994; Weimer, 1995]. We also adopt this format. For the presentations that follow, the velocity data were sorted in  $90^\circ$  sectors separated by  $45^\circ$  in the GSM  $y$ - $z$  plane. The intervals for sorting by IMF magnitude in the  $y$ - $z$  plane,  $B_T$ , were 0–4 nT, 4–6 nT, and 6–12 nT. The only sorting by  $Kp$  considered here spanned the interval  $2- \leq Kp \leq 3+$ .

## 4. Results

### 4.1. Potential Patterns

Figure 6 shows the set of patterns obtained for  $2- \leq Kp \leq 3+$ , that is, conditions typical of light-to-moderate geomagnetic activity. Following Weimer [1995], we measure the IMF angle,  $-180^\circ \leq \alpha \leq 180^\circ$ , with respect to the  $+z$  axis with the sign determined by the requirement that pure  $B_{y+}$  correspond to  $\alpha = 90^\circ$ . Most of the properties discussed in relation to Figure 5 are observed here through the full range of IMF orientation, although the case of dominant  $B_{z+}$  ( $\alpha = 0^\circ$ ) is more exceptional. The basic pattern is two-cell for all values of  $\alpha$ . The dusk cell carries more potential variation and covers a larger area. There is an obvious increase in the total polar cap potential drop with increasing magnitude of  $\alpha$  but no more than a small (<10%) dependence on the sign of  $\alpha$ , that is, the total potential drop is symmetric with respect to the sign of  $B_y$ . The sign of  $B_y$  strongly influences the shape of the pattern with the dusk cell becoming more round (crescent-shaped) with increasing  $B_{y+}$  ( $B_{y-}$ ) content and the overall pattern rotates toward earlier MLT for increasing  $B_{y+}$  content. For  $\alpha$  decreasing from  $90^\circ$  to  $0^\circ$ , that is, rotation of the IMF from  $B_{y+}$  to  $B_{z+}$ , the morning cell weakens almost to the point of disappearance and the dayside contours of the dusk cell become increasingly distorted, so much so that some sunward convection occurs for northward IMF.

In Figures 7–9 we present the patterns derived for several intervals of IMF magnitude. For the lowest interval of IMF magnitude (Figure 7), the patterns for all values of IMF angle are basically two-cell. The total potential variation ranges from 21 kV for northward IMF to 56 kV for southward IMF. For  $|\alpha| \geq 90^\circ$  (i.e., nonnorthward IMF) the area covered by the dusk cell and its associated potential variation exceed those of the dawn cell by approximately a factor of 2, while for  $|\alpha|$  decreasing to  $0^\circ$  these ratios increase. The patterns are generally rotated away from alignment with the noon-midnight meridian toward earlier MLTs such that the center of the dusk (dawn) cell is shifted sunward (antisunward) of the dawn–dusk meridian. Overall, the patterns are fairly featureless.

For IMF in the intermediate range of magnitude (Figure 8) some developments are apparent. The pure northward pattern has a reduced total potential drop (18 kV) while the potential drops for the patterns with  $B_{z-}$  content increase to a maximum of 68 kV for  $\alpha = 180^\circ$ . For  $|\alpha| \geq 90^\circ$  the relative enhancement of the dusk cell over the dawn cell in terms of area is reduced; for  $B_{z-}$  this reduction applies as well to the ratio of the potential variations. At this level of  $B_T$  the line connecting the cell centers for the  $\alpha = -45^\circ, -90^\circ$  patterns are counterrotated with respect to the usual shift toward earlier MLTs relative to the dawn–dusk meridian. For dominant  $B_{y+}$  the center of the dusk cell reaches 15 MLT.

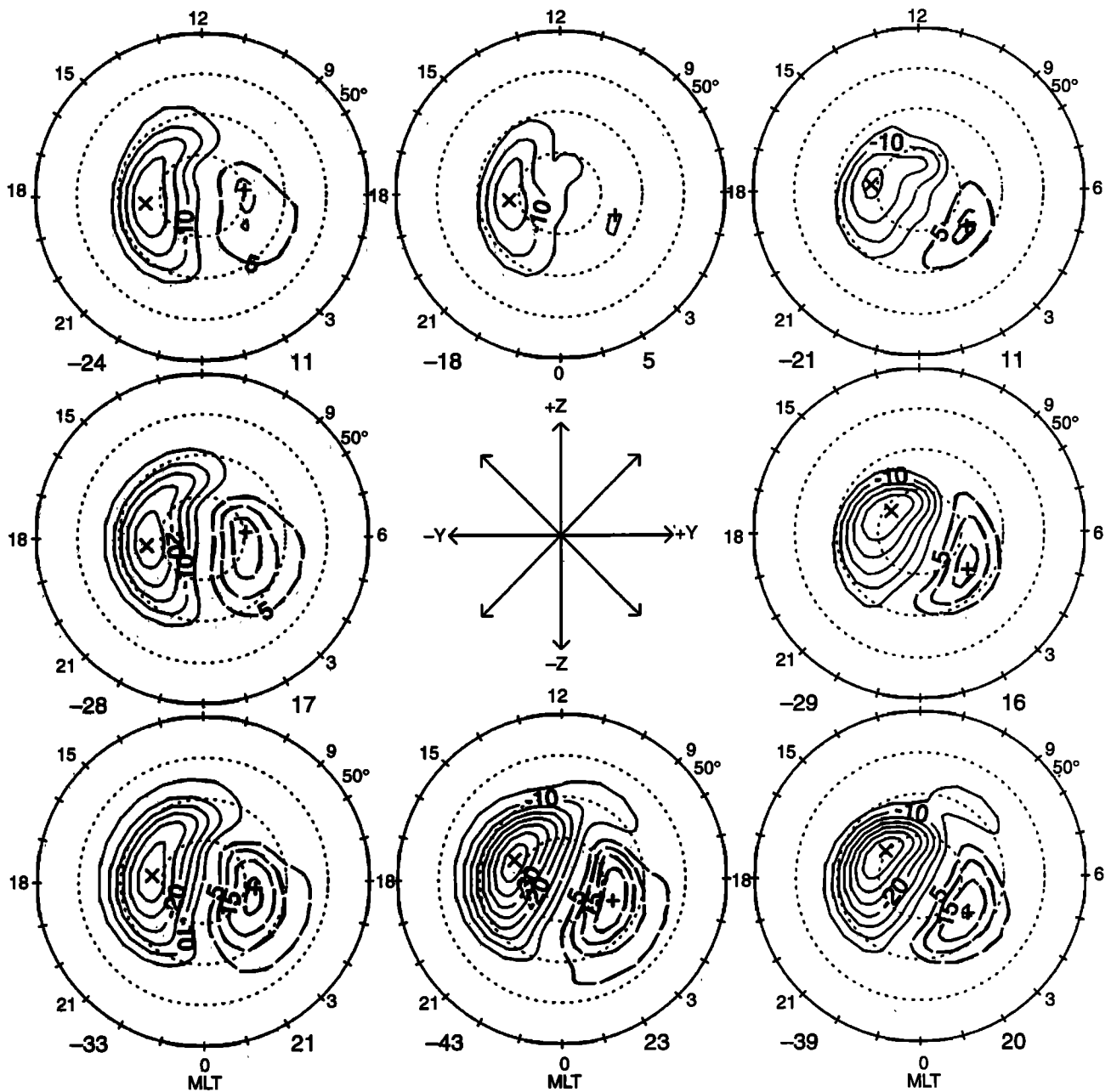


Figure 6. Convection patterns sorted by IMF angle for a moderate geomagnetic disturbance level ( $2- \leq Kp \leq 3+$ ). The potential extrema are shown as cross symbols (negative) and plus symbols (positive).

For the highest range of IMF magnitude (Figure 9) the variations in the patterns become extreme. The total potential drop in the  $B_z+$  case decreases to 15 kV while that for  $B_z-$  approaches 80 kV. For  $|\alpha| \geq 90^\circ$  the areas covered by the two cells are more similar than was the case for the lower intervals of  $B_z$ ; for the patterns with  $B_z-$  content in particular the dawn cell shows more comparable spatial extent and potential variation. The orientation of the line joining the cell centers and the direction of the polar cap flow are very sensitive to the sign of  $\alpha$ . For IMF strongly northward a weak counterrotating cell forms in the noon sector. There is a marked  $B_z$  asymmetry for  $|\alpha| < 90^\circ$ ; the  $B_z-$  pattern can be characterized simply as weakened two-cell while the  $B_z+$  pattern is more complex with evidence of multiple potential extrema.

We qualify our discussion of Figure 9 by noting that several effects of strongly southward IMF complicate the analysis. The first is the expansion of the system of convective flows to lower latitudes. More of the convection then occurs below the lowest latitude of direct radar observations ( $65^\circ\Lambda$ ) and the portion of the pattern solved by extrapolation is larger. Applying  $\Lambda_0 = 60^\circ$  can cause an unreasonable compression of the return flows along the flanks. We have consequently applied  $\Lambda_0 = 55^\circ$  to derive the three  $B_z-$  patterns. The second effect is a dropout in radar coverage in the dawn sector for extremely disturbed conditions as a result of increased HF absorption. This may be responsible for the weakening of the dawn cell in the  $\alpha = 180^\circ$  pattern relative to the  $\alpha = \pm 135^\circ$  patterns. Finally, for strong southward IMF conditions substorm activity can be expected to

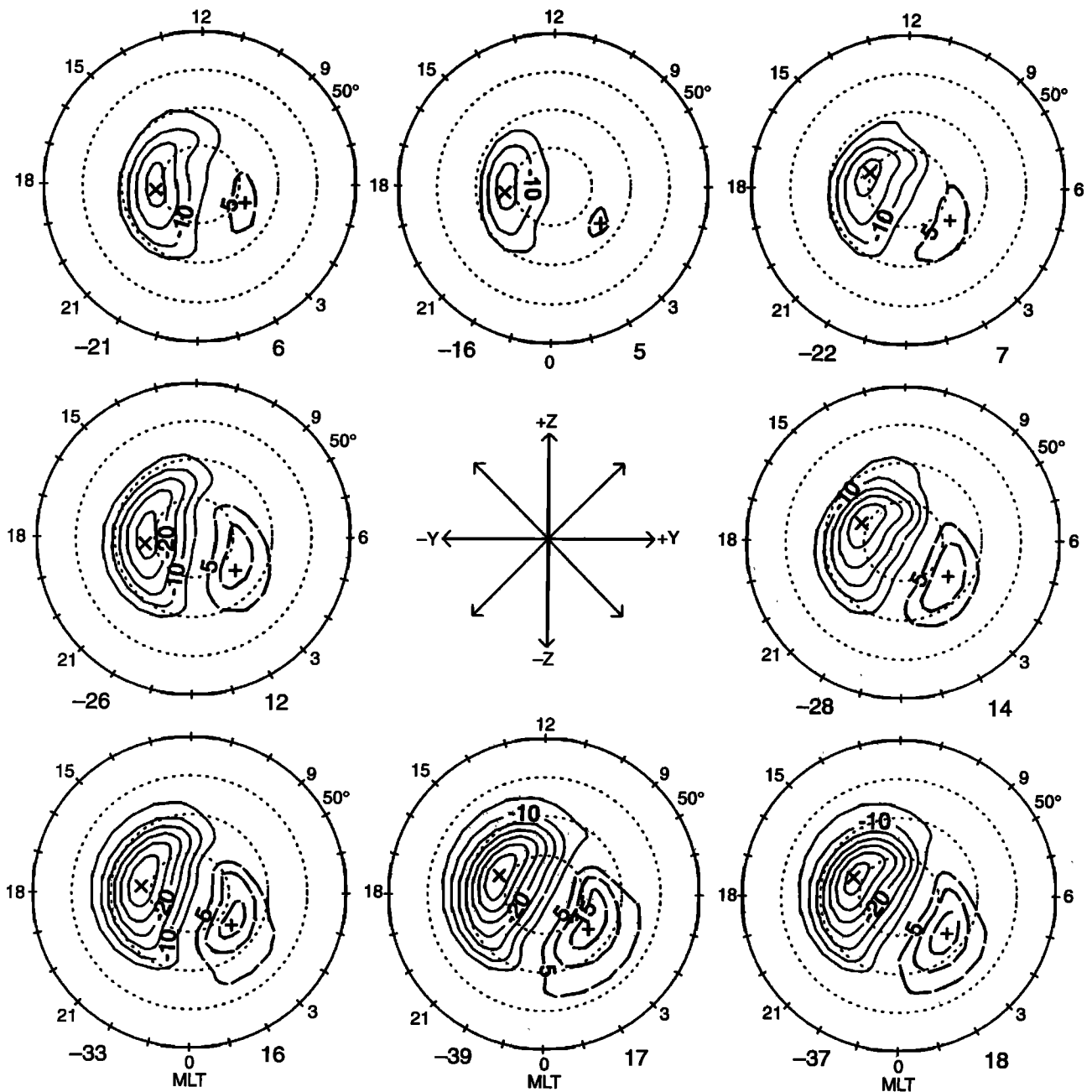


Figure 7. Convection patterns sorted by IMF angle for IMF magnitude in the interval  $0 \leq B_T \leq 4$  nT.

significantly perturb the potential distribution especially on the nightside [Shue and Weimer, 1994; Kamide et al., 1996]. The effect of mixing substorm phases in the statistical patterns is not clear. Thus the details of the patterns for stronger southward IMF are subject to greater uncertainties.

The case of large  $B_T$  with dominant  $B_z+$  is of particular interest. Figure 10 shows the clockdial plot obtained for  $\alpha = 0^\circ$  and  $B_T \geq 7$  nT. (The interval of the potential contour step has been reduced to show detail.) The two potential extrema lying near the noon meridian just above  $80^\circ\Lambda$  define a counterrotating two-cell structure. The dominant dusk cell envelops this structure while the weak dawn cell lies well to the nightside. The overall pattern is four-cell in character. In the region of reverse convection more potential variation is found across the prenoon cell. The progression through the levels of

$B_T$  for dominant  $B_z+$  suggests an evolution that begins with distorted two-cell convection, passes through three-cell with the emergence of a postnoon reverse convection cell, and concludes with four-cell for the most strongly northward IMF.

We conclude this discussion with an observation. In Figure 9 it appears that there may be some difficulty in resolving the extent of the dusk cell for  $B_z+$ . The main dusk cell is bounded on its equatorward side near 14 MLT by a weak counterrotating cell. The physicality of this cell is not clear; one could perhaps have accommodated the flows above  $65^\circ\Lambda$  in this area by simply incorporating them into an expanded dusk cell. The cell arises because more potential variation appears across the lower part of the dusk cell than is accommodated by the higher latitude portion in the optimal fitting of the velocity data to potential contours. Such potential offsets are

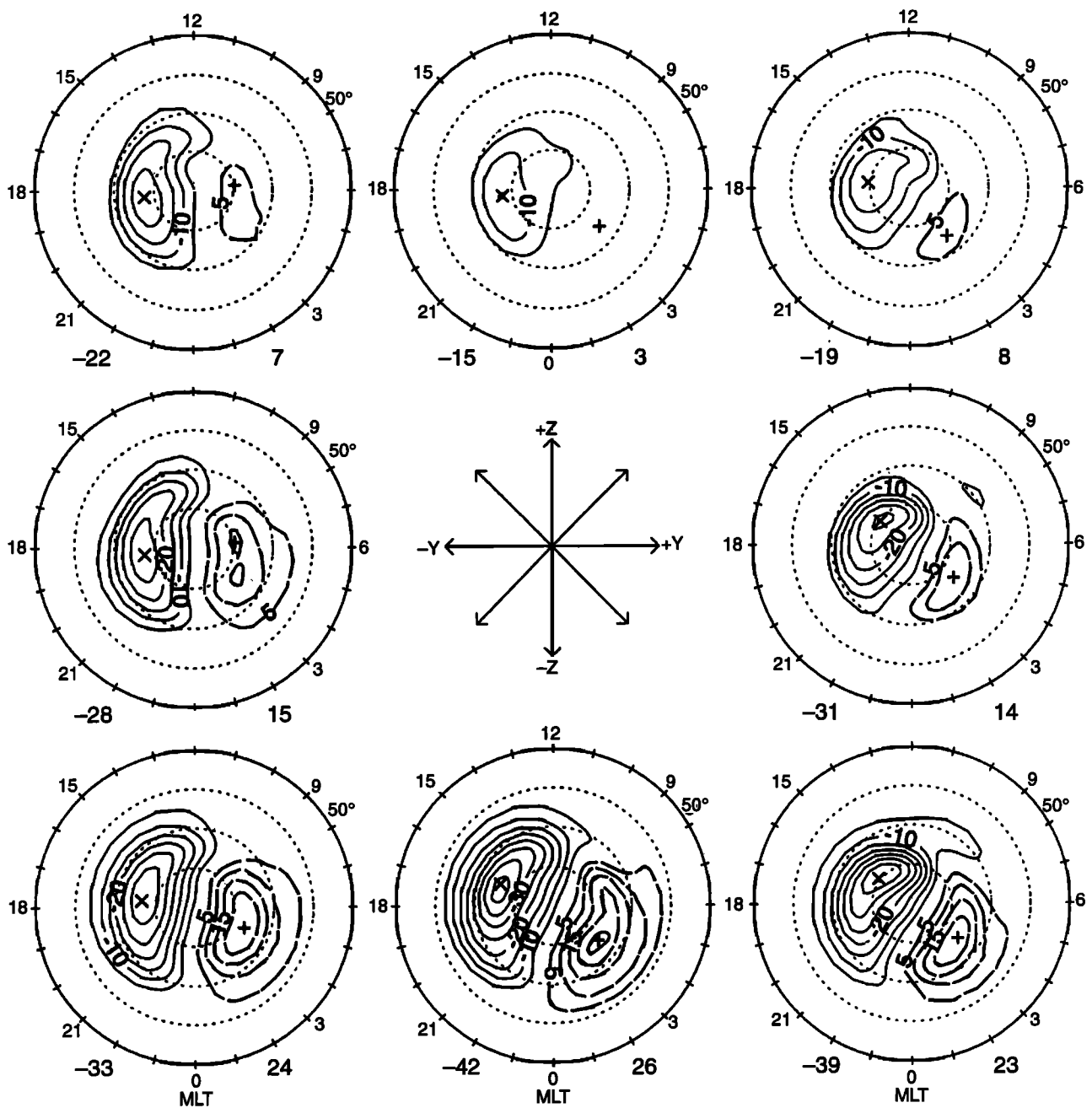


Figure 8. Convection patterns sorted by IMF angle for IMF magnitude in the interval  $4 \leq B_T \leq 6$  nT.

frequently encountered [e.g., *de la Beaujardière et al.*, 1991; *Weimer et al.*, 1995] and can be renormalized to zero by various means. We present these results with no adjustment. The peculiarity of this feature may point to unsuspected physical processes or to the limits of confidence in the technique applied here to map the global convection.

#### 4.2. Summary of IMF Dependencies

Here we summarize some of our findings on the IMF dependencies of high-latitude convection in the northern hemisphere. These points have either been discussed or are apparent from examination of Figures 5–9:

1. The convection is primarily two-cell. The notable exception occurs for strong northward IMF for which it is multicell.
2. The dusk cell is larger in terms of spatial extent and po-

tential variation. The cells are more equal for increasing  $B_y$ -content. The dusk cell tends to extend over the noon meridian at auroral latitudes.

3. The  $B_y$  effect can be characterized as globally coherent in the sense that the flow deflections are consistent with a global ordering of the basic two-cell convection pattern on the basis of cell shape and pattern orientation in MLT. For  $B_y^-$ , the dusk cell is more crescent-shaped and the orientation of the pattern is such that flow in the polar cap is antisunward and the line joining the cell centers is nearly aligned with the dawn–dusk meridian. For  $B_y^+$ , the dusk cell is more round and the orientation of the overall pattern is such that the polar cap flow has a significant inclination (prenoon to premidnight) and the cell centers are shifted to earlier MLTs.

4. The  $B_z$  effect is seen on the nightside. As  $B_z$  changes sign, the rounder cell becomes crescent-shaped and shifts to-

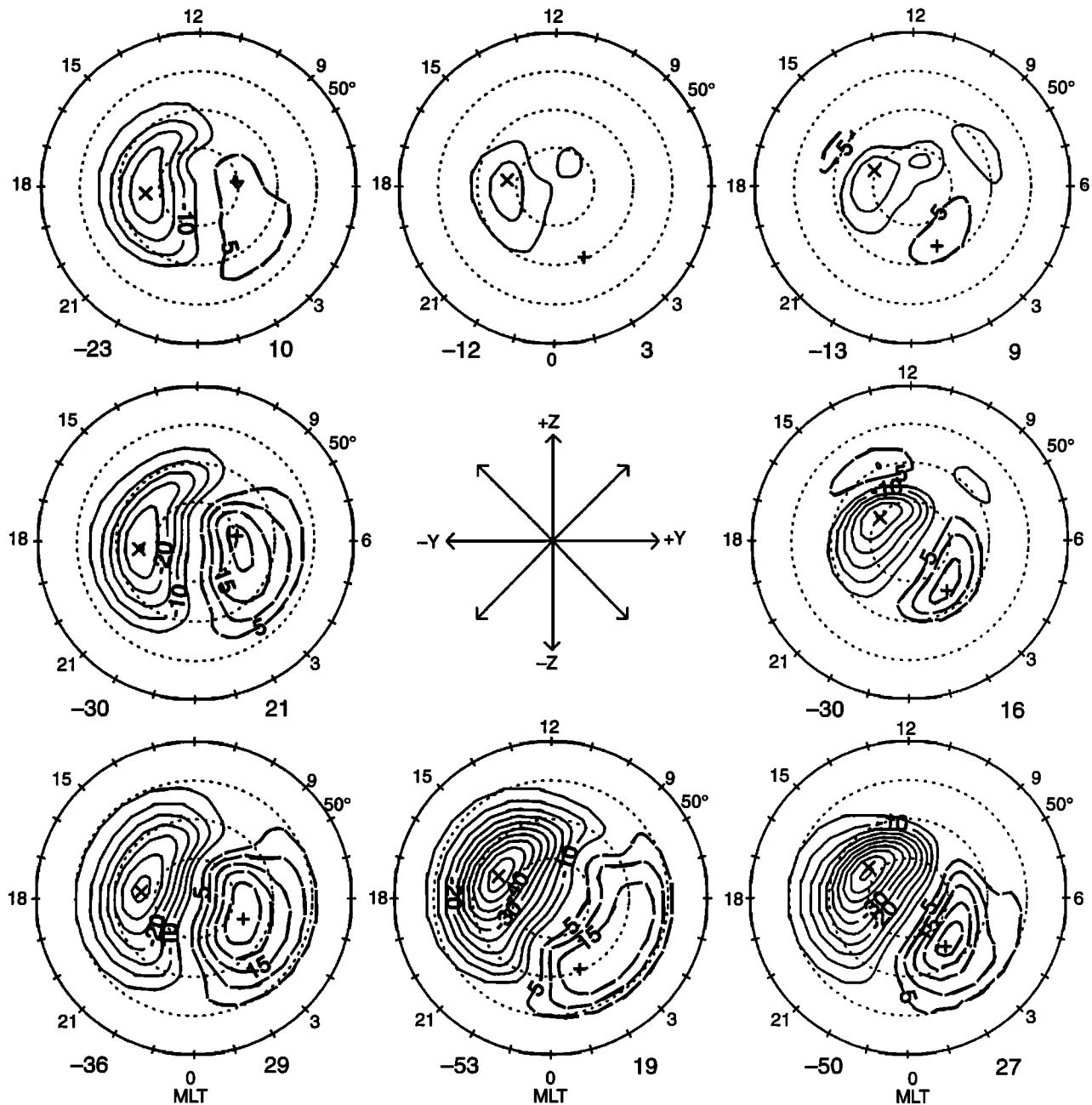


Figure 9. Convection patterns sorted by IMF angle for IMF magnitude in the interval  $6 \leq B_T \leq 12$  nT.

ward the midnight meridian. The zero potential line rotates significantly ( $\sim 2$  hours) in MLT and is encountered earlier for  $B_y+$ . The more extreme geometry is obtained for  $B_y+$  for which the midnight sector is dominated by the crescent-shaped dawn cell. In terms of convection reversals, for example, the Harang discontinuity, a distinct feature can be discerned only in the sector of the crescent-shaped cell, that is, premidnight for  $B_y-$  and postmidnight for  $B_y+$ .

5. For strongly northward IMF, the pattern is four-cell with two small reverse convection cells at high latitudes on the day-side. The prenoon reverse convection cell is stronger and may emerge first with increasing  $B_z+$ , generating an intermediate three cell pattern. The reverse convection cells are enveloped by the dusk cell and the dawn cell is comparatively weak.

#### 4.3. Comparison With Previous Ground-Based Studies

The foregoing results can be compared with a sizable body of previous work dealing with the statistical characterization of high-latitude convection. In this section we review some of the findings derived from ground-based observations. The principal techniques employed in this earlier work were radars and magnetometers.

An early statistical model was derived by Foster [1983] on the basis of incoherent scatter observations collected with the Chatanika radar. Nine days of data gathered under predominantly  $B_y-$  conditions were used to map convection in the  $58^\circ$ – $75^\circ$ A interval. The dusk cell was found to be larger both in terms of area and potential variation. We have found that the dusk cell is dominant for all values of  $\alpha$ .

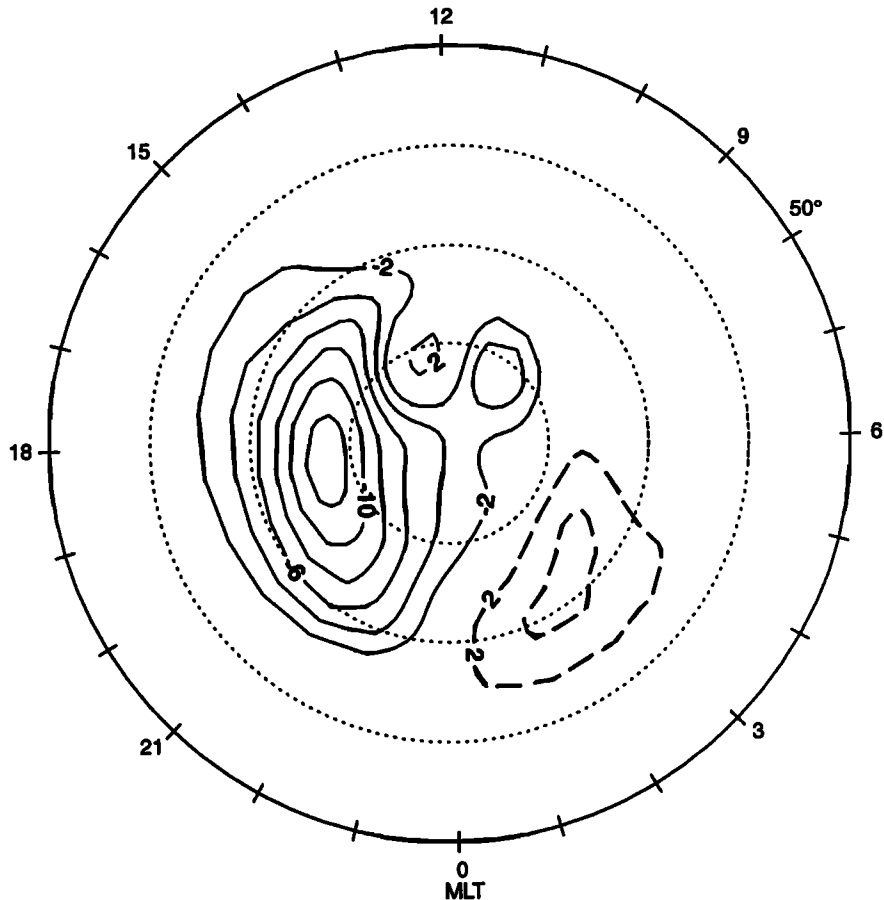


Figure 10. Convection pattern for northward IMF and IMF magnitude in the range  $B_T \geq 7$  nT.

After the Chatanika radar was relocated to Sondrestrom, Greenland, convection could be studied over the  $68^\circ$ – $82^\circ\Lambda$  interval. In a case-by-case examination [de la Beaujardière *et al.*, 1985] and a more statistical analysis [de la Beaujardière *et al.*, 1986] of 14 days of observations, a  $B_y$  effect was reported in the nightside convection. For  $B_y+$  ( $B_y-$ ) their velocity maps show more latitudinal velocity shear in the postmidnight (premidnight) sector and the most pronounced feature in the midnight-to-early morning sector is a region of westward velocity above  $75^\circ\Lambda$  for  $B_y+$ . These characteristics are consistent with the nightside  $B_y$  effect described here.

The incoherent scatter radar at Millstone Hill has also been utilized for convection studies. Its field of view extends from midlatitudes to approximately  $75^\circ\Lambda$ . IMF dependencies were considered by Foster *et al.* [1986b] and Holt *et al.* [1987], who analyzed ~100 days of observations. Holt *et al.* [1987] schematically closed flow contours over the polar cap while Foster *et al.* [1986b] qualitatively adapted the model of Heelis [1984] to complete the global mapping. A variation of the potential drop from ~15 kV for  $B_z+$  to ~75 kV for  $B_z-$  for IMF of moderate magnitude was reported. They also described overall domination by the dusk cell and a  $B_y$  factor on the nightside such that the dawn (dusk) cell makes a larger contribution to the convection on the midnight meridian for  $B_y+$  ( $B_y-$ ). These qualitative properties are found in the model developed here. A possible explanation for the weakness of the dayside  $B_y$  effect in the maps of Holt *et al.* [1987] is that the strongest dayside  $B_y$  effects are found at higher latitudes ( $>75^\circ\Lambda$ ) than were di-

rectly observed by the Millstone Hill radar and the return flows of the dusk cell dominate the noon sector at lower latitudes for both signs of  $B_y$ .

Senior *et al.* [1990] describe a statistical model derived from incoherent scatter observations carried out with the EISCAT facility located in Scandinavia. The coverage extends over the  $61^\circ$ – $73^\circ\Lambda$  interval and sorting is only by  $K_p$  so that a comparison of IMF factors is not possible. They do, however, find a persistent rotation of the overall two-cell pattern toward earlier MLTs, consistent with the usual sense of rotational offset described here. Interestingly, they find much less predominance of the dusk cell in terms of spatial extent and potential variation than is the case for studies carried out in the American sector.

The technique of coherent scatter has also been previously applied to the study of high-latitude plasma convection. Scourfield and Nielsen [1981] used 14 days of observations with the STARE radar to study the  $B_y$  dependence of the nightside reversal in the zonal velocity near  $71^\circ\Lambda$ . They found an earlier reversal for  $B_y-$ . We have described a shift of the opposite sense in the MLT of the zero potential line; possibly they detected the movement of the Harang discontinuity across their field of view in the premidnight sector for  $B_y-$ . Waldock *et al.* [1985] used 380 days of measurements from the SABRE facility to investigate  $K_p$  dependencies in the  $61^\circ$ – $67^\circ\Lambda$  interval. Jones [1989] used nearly 800 hours of SABRE data and observed a strong  $B_y$  influence near  $64^\circ\Lambda$  consisting mainly of a shifting of the position of the nightside reversal in the zonal

flow to earlier MLT for  $B_y+$ . This is consistent with the shifting of the zero potential line on the nightside that we have described (the SABRE observations apparently did not extend across the Harang discontinuity in the  $B_y-$  case). Less of a  $B_y$  effect was observed on the dayside, probably owing to the lack of variability over this latitude range as discussed earlier in relation to the Millstone Hill results. In a case study, *Dudeny et al.* [1991] found evidence of a  $B_y$  dependence in nightside convection observed with the Halley HF radar. In a statistical study incorporating Halley observations collected over a 2-year period, *Leonard et al.* [1995] sorted by the signs of the IMF components. They confirmed that on the dayside the southern hemisphere flows are antisymmetric to those in the northern hemisphere with respect to the sign of  $B_y$ . As we have discussed, this antisymmetry applies as well to the flows on the nightside. The orderly transition in the latitude of the nightside flow reversal in the evening sector known as the Harang discontinuity is clear only for the sign of  $B_y$  that produces a crescent-shaped cell in the dusk sector, namely,  $B_y-$  for the northern hemisphere and  $B_y+$  for the southern hemisphere. For the other sign of  $B_y$ , latitudinal velocity shear is concentrated in the dawn sector. A nightside  $B_y$  effect in the Goose Bay HF radar observations was first discussed by *Ruohoniemi and Greenwald* [1995]. Here we have shown that it arises from a globally coherent modulation of high-latitude convection by  $B_y$ .

Magnetometer measurements have also been used to derive statistical models of high-latitude electric fields. *Berthelier et al.* [1974] examined arctic and antarctic observations to show the basic  $B_y$  dependence of the high-latitude current patterns and their hemispheric asymmetry. *Friis-Christensen et al.* [1985] analyzed summer data collected with a chain of magnetometers on the west coast of Greenland, and *Papitashvili et al.* [1994] subjected data collected in both hemispheres to a regression analysis that included a seasonal sorting. The magnetometer technique for inferring the electrostatic potential distribution is somewhat indirect since a model of the ionospheric conductivity must be applied to deconvolve this information from a distribution of geomagnetic perturbations. Although a  $B_y$  effect is obtained in the magnetometer-based models, it is surprising that the dawn cell tends to be dominant. It is considerably larger in spatial extent than the dusk cell in the patterns of *Friis-Christensen et al.* [1985]. In the IZMEM model, the potential variation across the dawn cell is 2–4 times greater than that across the dusk cell for dominant  $B_z-$  in equinoctial-winter conditions (V. O. Papitashvili, private communication, 1995). This relationship of cell magnitudes is the opposite of that reported here and in other studies. The patterns of *Friis-Christensen et al.* [1985] show relatively little variation of the orientation of the two-cell pattern such that the dusk cell dominates the noon meridian and the dawn cell dominates the midnight meridian, that is, a nightside  $B_y$  effect is not seen. In the IZMEM model there is a strong sign dependence in the  $B_y$  dominated patterns and a nightside effect, but this is muted in the patterns with  $B_z-$  content for which the predominance of the dawn cell tends to extend to both the noon and midnight meridians. For  $B_z+$  both magnetometer models indicate that the dawn cell is dominant, while we find that it is greatly diminished. The greater consistency found within the magnetometer technique may indicate a persistent shortcoming of the conductivity models.

#### 4.4. Comparison With Satellite Studies

Magnetospheric convection has been studied with instruments carried by satellites since the sixties [e.g., *Maynard and Heppner*, 1970]. The effect of IMF variations on dayside convection was noted by *Heppner* [1972] and found to be in substantial agreement with the findings of the magnetometer-based studies. An extensive set of measurements was compiled by *Heelis* [1984] and used to formulate an empirical model of dayside convection. Subsequent analyses of satellite data rendered additional models [*Burch et al.*, 1985; *Heppner and Maynard*, 1987]. The recent works of *Rich and Hairston* [1994] and *Weimer* [1995] constitute the most detailed satellite-based models of global convection to date.

In the schematic model of *Heelis* [1984], derived from observations with the Atmosphere Explorer C satellite, the dayside convection is structured mainly by the orientation of the zero-potential line that divides the flow into dawn and dusk cells. This line was found to be displaced toward dawn irrespective of the sign of  $B_y$ , a result that is consistent with the general tendency for the dusk cell to be larger and to extend across the noon meridian. At higher latitudes flows in the model are directed toward dusk for  $B_y-$  and toward dawn for  $B_y+$ , consistent with the  $B_y$ -dependent shaping of the dayside convection into round and crescent-shaped cells.

Simplified schematic plots of  $B_y$ -dependent convection were derived by *Burch et al.* [1985] on the basis of dayside observations from Dynamics Explorers 1 and 2 and dynamical considerations. Besides the round/crescent cell splitting of the global pattern, their model predicts for strong  $B_y$  the existence of a pair of east–west convection reversals on the duskside (dawnside) at auroral latitudes for  $B_y+$  ( $B_y-$ ). These reversals are not apparent in our patterns. The concepts developed by *Burch et al.* [1985] to explain the basic  $B_y$  dependencies were generalized to arbitrary IMF orientation by *Reiff and Burch* [1985]; we make comparisons with this theory in the next section.

*Heppner and Maynard* [1987] utilized data from the DE 2 satellite to synthesize schematic global convection patterns. For  $B_z-$  they presented two patterns characteristic of  $B_y+$  (A, DE) and one for  $B_y-$  (BC) scaled for moderately disturbed conditions ( $3+ \leq Kp \leq 4-$ ). These show the dominance of the dusk cell in potential variation, although the dusk cell covers more area in the DE pattern. (The A pattern is a better match to our  $B_y-$  results, as the DE pattern shows the cross polar cap flow concentrated excessively on the duskside and a dawnward component to the flow at the pole.) The Heppner and Maynard patterns split into generally rounder and more crescent-shaped cells on the dayside with a polarity that depends on the sign of  $B_y$ . Besides these similarities, we find differences between our results and those of Heppner and Maynard. Generally, the latitudinal velocity shears are more extreme in the H-M patterns; the changes in the zonal velocity along a streamline mostly occur within limited ( $< 4^\circ$ ) latitude intervals. Some of the differences in the scale of the structure is undoubtedly due to the “pattern-recognition” basis of the Heppner-Maynard study versus the “bin-averaging” approach taken here. For the  $B_y-$  case, the A pattern shows a shift of the line joining the cell centers to earlier MLTs, while we have found approximate alignment with the dawn-dusk meridian or even counterrotation. For the  $B_y+$  case the positions of the cell centers in both models are ro-

tated to earlier MLTs by several hours. However, the descriptions on the nightside are then particularly inconsistent; the BC pattern shows latitudinal velocity shear in the premidnight sector consistent with a clear Harang discontinuity feature and on the midnight meridian the polar cap flow with its duskward component rotates sharply to dawnward just above  $70^\circ\text{A}$ . The net result is that below  $70^\circ\text{A}$  there is little difference between the Heppner and Maynard  $B_{y+}$  and  $B_{y-}$  patterns. The latitudinal range of insensitivity to the sign of  $B_y$  would be even larger for less disturbed conditions. This insensitivity is contrary to our findings (e.g., Figure 5) and to those of other ground-based studies, most notably Leonard *et al.* [1995].

For northward IMF, there is partial agreement with Heppner and Maynard in terms of the evolution of the two-cell pattern with increasing  $B_z+$  content, namely, the potential extrema associated with the dusk cell shift to earlier MLTs and finally cross the noon meridian, generating sunward flow at high latitudes on the dayside. However, Heppner and Maynard accommodate this development by distorting the contours of the two-cell pattern while we have found a better statistical fit to a multicell pattern. Furthermore, for strong  $B_z+$  the patterns of Heppner and Maynard show a dawn cell that is comparable on the nightside to the dusk cell, while we have noted an asymmetrical weakening of the dawn cell with increasing  $B_z+$ . A possible source of this discrepancy lies in the filtering that was applied by Heppner and Maynard who dropped cases where widespread irregularity in the convection obscured pattern recognition. Weak, irregular flow is especially characteristic of the winter hemisphere under  $B_z+$  conditions [e.g., Lu *et al.*, 1994]. Our patterns represent the average state of this convection while those of Heppner and Maynard are perhaps more characteristic of that subset of events for which the convection was more highly ordered.

The recent satellite-based studies by Rich and Hairston [1994] and Weimer [1995] provide the most complete references for comparison. Such comparison constitutes a demanding intercalibration of the space- and ground-based analyses. In this section we assume that the reader is familiar with the principal results reported in these papers.

Rich and Hairston [1994] analyzed several years of drift data collected with DMSP satellites. Comparison with their results is somewhat hampered by differences in our parameterization of the convection; they sorted simultaneously by IMF orientation in the  $y$ - $z$  plane, three-dimensional IMF magnitude (not  $B_T$ ), and season (not done here). However, we note that their winter and equinoctial patterns are very similar and that our statistics are dominated by measurements made in the winter and equinoctial months. Also, we can roughly reconcile their characterization by IMF magnitude with our  $B_T$  sorting by matching the levels of potential variation in the patterns. These considerations indicate that the most suitable comparisons are between our Figures 8 and 9 ( $4 \leq B_T \leq 6$ ,  $6 \leq B_T \leq 12$  nT) and their Figures 4 and 6 (winter and equinox with IMF magnitude in the range  $5 < |B| < 11$  nT).

Overall, the agreement is quite good. For nonnorthward IMF, that is,  $|\alpha| \geq 90^\circ$ , the two cells in the Rich and Hairston patterns occupy similar areas and show the same overall rotation with increasing  $B_{y+}$  content and a similar division of the total potential drop between the two cells. The dusk cell dominates the noon meridian, and the general  $B_y$  dependence on the nightside is similar to that reported here. There are significant differences, however. In terms of grosser structure, the cells tend to be more elongated in the patterns of Rich and Hairston.

At smaller scales, some of the streamlines in the Rich and Hairston patterns follow highly convoluted paths. This is likely due in part to the free-hand drawing of contours in the Rich and Hairston analysis. While such an approach offers potentially higher spatial resolution, the physicality of some of the resolved structure is not clear. For example, in Figure 6 of Rich and Hairston some streamlines that extend through the polar cap change direction on the nightside by  $\sim 90^\circ$  over very limited ( $< 2^\circ$ ) latitude intervals. Rich and Hairston concluded that there was not a strong nightside feature corresponding to the classical Harang discontinuity for either sign of  $B_y$ .

The patterns for northward IMF also have similarities. The dusk cell is dominant and secondary potential extrema on the dayside lead to sunward convection. At smaller scales, the case of strongest  $B_z+$  (Rich and Hairston, Figure 7, top) suggests an enveloping dusk cell and the near-disappearance of the dawn cell. However, the pattern shows multiple secondary extrema and does not conform to a predominant four-cell morphology like that of Figure 10. The differences are perhaps due to methodology; Rich and Hairston resolve the convoluted flow geometry for strong  $B_z+$  by drawing small-scale twists in the streamlines and multiple small cells, while our analysis resolves the situation by generating 1 or 2 counterrotating dayside cells.

The model of Weimer is based on measurements with the DE 2 satellite. The sorting intervals he chose are more directly comparable to those used here. His Figures 2–5 correspond to increasing magnitude of  $B_T$  analogous to the development in our Figures 7–9. We performed similar filtering of our data sets by the selection of finite orders in the series expansion of the potential; hence the levels of structure in the patterns are comparable. We find essential agreement over a wide range of parameters, even stronger than that in the comparison with Rich and Hairston. In the case of the lowest intervals of  $B_T$ , not only are the cells similarly shaped and positioned, but the potential variations are very nearly the same for all values of IMF angle. Figure 11 shows the set of patterns obtained by Weimer for  $B_T$  in an intermediate range. This can be compared most directly with the set of Figure 8. The patterns match in many details. We note some differences. The cells in Weimer extend to somewhat lower latitude. More surprisingly, the line joining the cell centers shows the most counterrotation in the Weimer patterns at  $\alpha = -135^\circ$ , not for dominant  $B_{y-}$  ( $\alpha = -90^\circ$ ). For dominant  $B_z+$  both patterns agree on the size and placement of the dominant dusk cell and the comparative weakness of the dawn cell but Weimer depicts a weak secondary cell on the dayside. This is perhaps only marginally significant as the Weimer pattern for the next level of  $B_T$  does not show such fine structure.

With increasing  $B_T$  the similarities in the gross details mostly remain. As one demonstration, we note that the double-peaking of the dusk cell in the  $\alpha = 45^\circ$  pattern of Figure 9 is reproduced in Weimer (Figure 5). For the case of dominant  $B_z+$  we both describe a weak pair of counterrotating cells with more potential variation across the prenoon cell. We also agree that while the patterns for  $\alpha = 0^\circ$  and  $\alpha = 45^\circ$  are topologically distinct because of structure in the dusk cell the pattern for  $\alpha = -45^\circ$  can be characterized simply as weakened two-cell. We note the following differences; the mismatch in terms of the  $B_y$ -dependent rotation of the overall pattern that increases with  $B_T$ , differences in some potential extrema, and the emergence of low-latitude counterrotating cells only in our patterns for  $B_{y+}$ . In addition, for the case of strong  $B_z+$  the dayside prenoon potential extremum connects to the larger dusk cell via

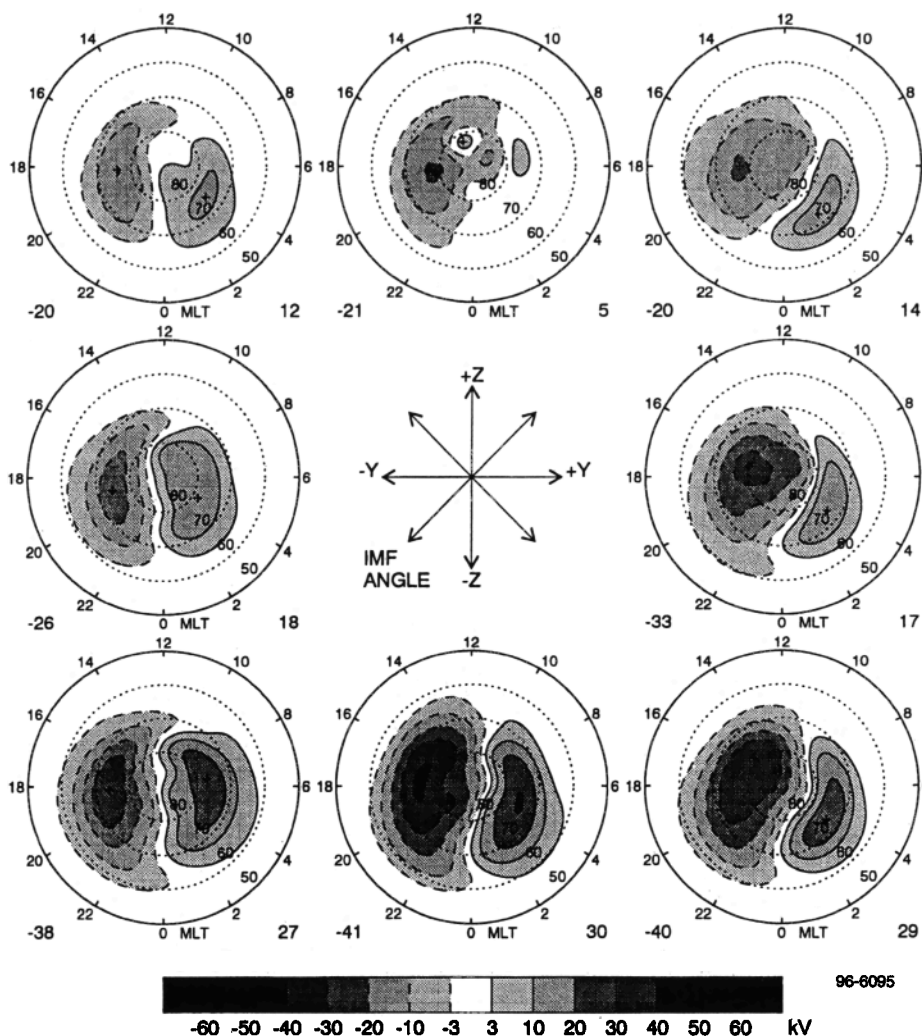


Figure 11. Contour graphs of electric potential sorted by IMF angle for IMF magnitude in the range  $3.5 < B_T < 5.2$  nT [from Weimer, 1995].

higher latitudes in our model (Figure 10) than in Weimer (Figure 5, top center).

In summary, we find very good agreement with the results of the recent satellite studies of global convection. This agreement is obtained despite wide differences in technique and analysis and boosts confidence in the validity of the statistical models. Some of the differences that remain, for example, modified two-cell convection for IMF strongly northward in Rich and Hairston versus multicell convection here and in Weimer, are perhaps best resolved by appeal to case studies. Regarding the multicell controversy, Greenwald et al. [1995a] recently described the formation of a counterrotating dayside cell during a period of extended  $B_z+$ ; the position and potential variation associated with the cell are a good match to the extreme  $B_z+$  scenario described here and in Weimer. Evidence of an event of multicell convection has also been advanced by Reiff and Heelis [1994].

### 5. Discussion

The convection of ionospheric plasma due to the interaction of the solar wind with the magnetosphere was interpreted by Axford and Hines [1961] in terms of a viscous-like diffusion

process, while Dungey [1961] invoked merging of the IMF with geomagnetic field lines under  $B_z-$  conditions. The merging mechanism was subsequently extended to  $B_z+$  conditions by Dungey [1963]. Development of the merging concept have been reviewed by Crooker and Rich [1993]. Briefly, the viscous interaction transfers momentum and energy from the streaming solar wind to plasma on the flanks of the magnetosphere. Small ( $< 10$  kV) kidney-shaped “viscous” cells form on closed field lines. For merging under  $B_z-$  conditions, dayside geomagnetic field lines reconnect with the magnetic field carried by the solar wind, transferring closed flux to open flux that is entrained by the antisunward solar wind motion. Merging in the magnetotail recloses the field lines. In the resulting “merging” cell the circulation is generally antisunward in the polar cap and sunward at auroral latitudes. Under  $B_z+$  conditions merging takes place at points poleward of the cusp; possible scenarios are discussed in the next section. A third category of interaction is associated with the tail lobes where the field lines have previously been opened [Russell, 1972]. Under appropriate conditions, the IMF merges with lobe field lines and drives a continual circulation of polar cap plasma. The sense of the circulation in the “lobe” cell is mainly determined by the IMF  $B_y$  component.

Conceptual models of IMF-dependent high-latitude convection have been developed and refined on the basis of these concepts [Crooker, 1979; Burch *et al.*, 1985; Reiff and Burch, 1985; Crooker, 1992]. Direct comparison with our patterns is complicated by several factors. First, the conceptual models are expressed in the inertial reference frame defined by the Sun-Earth geometry while the empirical convection patterns are expressed in a corotating reference frame. Because the motion associated with corotation is azimuthally unidirectional, a conceptual model that is mirror-symmetric with respect to  $B_y$  sign in an inertial frame will not have this symmetry in a corotating frame. The problem of comparing convection patterns in the two reference frames was considered by Maynard *et al.* [1995] for the model of Heppner and Maynard [1987]. The principal effects of transforming from corotational to inertial coordinates under  $B_z^-$  conditions were a greater equivalence in the sizes of the cells and a shift of the zero potential line on the dayside toward noon. These considerations indicate that some of the asymmetries reported here (cell size, pattern orientation, dusk-cell dominance of the noon meridian) would be diminished in an inertial mapping.

Second, the conceptual models are determined primarily by the geometrical conditions at the solar-wind-magnetosphere boundary. However, the ionosphere may significantly perturb the convection potential distribution through its loading effect on the magnetospheric emf source. The influence of the day-night conductivity gradient on convection trajectories was analyzed by Atkinson and Hutchison [1978]. The primary effect is the deflection of convective flow toward the dawnside, resulting in a larger and rounder dusk cell. As discussed by Crooker and Rich [1993], the day-night conductivity gradient breaks the mirror symmetry of the  $B_y$  patterns, rendering a more extreme configuration for  $B_{y+}$  in the northern hemisphere. This ordering is consistent with our results. However, the conductivity-gradient effect has not yet been incorporated into the conceptual models in a rigorous manner and this may explain some of the discrepancies with the empirical models. In the following, we limit the discussion of the comparison with conceptual models to those features of the convection that are not obviously a consequence of the inertial mapping or conductivity gradient factors.

The model of Crooker [1979] predicts the morphology of the convection on the dayside as a function of angle in the  $y$ - $z$  plane. Dayside merging occurs along the line where the IMF and the geomagnetic field are antiparallel and the associated plasma acquires antisunward motion normal to this line. The model predicts two merging cells for  $B_z^-$ , one crescent-shaped and the other round. The crescent-shaped cell lies on the dawn side in the northern hemisphere for  $B_{y+}$ . This study and most others have found this effect [e.g., Heelis, 1984; Papitashvili *et al.*, 1995]. The degree of crescent/round cell shaping of the global pattern has not been entirely clear; as noted previously, Heppner and Maynard [1987] did not find a pronounced  $B_y$  effect at lower latitudes on the nightside. We have found, however, that the  $B_y$  effect does extend to the nightside, chiefly through the rotation of the zero potential line in MLT and shaping of the cells. Comparison with Leonard *et al.* [1995] indicates that the nightside factor is hemispherically antisymmetric. We can thus qualitatively extend the dayside patterns of Crooker [1979] for  $B_z^-$  to the nightside by applying the global coherence of the  $B_y$  effect.

The Crooker [1979] model predicts that convection for  $B_z^+$  is dominated by circulation within a single large rounded lobe

cell with the sector and sense of circulation selected by the sign of  $B_y$ . Our patterns do not support this scenario; convection in the dawn sector is weak even for  $B_{y-}$  and the sunward component of the dayside flows appears restricted to a small region of highly structured convection. Further developments of the model for  $B_z^+$  conditions as described by Crooker [1992] indicate that the merging geometry in the  $x$ - $z$  plane leads to the formation of lobe cells only in the summer (or  $B_x$ -favored) hemisphere. Although seasonal (or  $B_x$ ) factors are beyond the scope of this study, we have found some evidence of this behavior in our database.

Reiff and Burch [1985], building on the analysis of Burch *et al.* [1985], synthesized a conceptual model of high-latitude convection incorporating all three types of convection cells. For  $B_z^-$  conditions, their model predicts a configuration in the dayside merging region similar to that of Crooker [1979] but modifies the convection elsewhere with the addition of viscous and lobe cells. The viscous cells are nested in the merging cells while a single lobe cell circulates on the duskside (dawnside) of the polar cap for  $B_{y+}$  ( $B_{y-}$ ). Two reversals occur in the zonal velocity along the dawn-dusk meridian in the sector of lobe cell circulation, one at the potential extremum in the viscous cell and the other at the open-closed field line boundary that separates the viscous and lobe cells. We do not find evidence of the existence of such a double reversal. Elimination of either the lobe or viscous cell in the  $B_y$ -selected sector would eliminate the inconsistency. It is interesting that Lu *et al.* [1994] found in their event study that the viscous cell adjacent to the lobe cell was often too small to be recognized. The suppression of the viscous cell in the sector of lobe cell circulation under  $B_z^-$  conditions might thus be a general property.

For  $B_z^+$ , the Reiff and Burch model predicts that the merging cell circulation gives way to a strongly  $B_y$ -dependent lobe cell, culminating in two symmetric reverse convection lobe cells for strong  $B_z^+$ . The lobe cell circulation is bounded at lower latitudes by two viscous cells. As before, it is difficult to reconcile this evolution of the pattern with increasing  $B_z^+$  with our observations; while some lobe cell characteristics are perhaps obtained for  $B_{y+}$  the situation of a dominant dusk cell for  $B_{y-}$  is clearly a problem (e.g., Figure 9). Of course, if lobe cell formation is restricted to the summer (or  $B_x$ -favored) hemisphere, the model of Reiff and Burch [1985] for  $B_z^+$  would not be a valid representation of average winter (or average  $B_x$ -unfavored) conditions. An inconsistency then arises because the model predicts that the winter (or  $B_x$ -unfavored) hemisphere is left in a near-dormant condition while we have observed well-ordered (if somewhat weak) reverse convection.

An interesting comparison can be made for the case of extreme northward IMF with the results of Rasmussen and Schunk [1987], who modeled numerically the effect of an NBZ current system on convection in the polar regions. Figure 12 shows the solution they obtained for the potential distribution assuming a simple system of region 1 and NBZ Birkeland currents and an equinoctial day-night gradient in ionospheric conductivity. Note that the field-aligned current model used as input was symmetric about both the noon-midnight meridian and the dawn-dusk meridian. The effect of the realistic conductivity distribution is to enhance the prenoon reverse convection cell and the normal dusk cell. This pattern can be compared with the statistical result for extreme  $B_z^+$  shown in Figure 10. Given that the potential can be scaled arbitrarily in the model, the agreement is very good. In particular the dawn cell is relatively

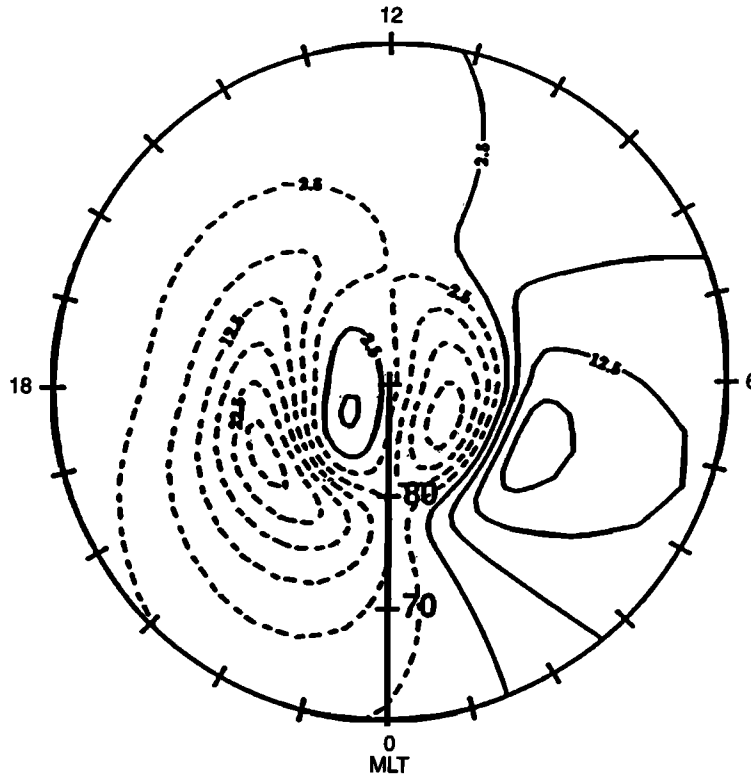


**Figure 12.** Plot of the ionospheric electric potential assuming a numerical model of the NBZ Birkeland currents and a realistic conductivity distribution [from *Rasmussen and Schunk, 1987*].

weak and the dusk cell envelops the pair of small counterrotating cells. Incorporating such realistic effects into the model as a sunward shift of the currents representing the NBZ system [*Iijima et al., 1984*] and a clockwise rotation of the overall pattern would further enhance the comparison. The validity of this comparison implies that the ionospheric load heavily modifies the potential distribution imposed by the magnetospheric generator, at least for  $B_z+$  conditions. Models based solely on the dynamics of the solar wind-magnetosphere interaction do not incorporate such effects and will be less effective in reproducing observations.

There is a question as to the source of the convection for the dawn and dusk cells for extreme  $B_z+$ . The potential variation obtained across the dusk cell is  $\sim 14$  kV while that across the dawn cell is  $\sim 5$  kV. A variation of  $\sim 10$  kV is expected of the viscous interaction along a magnetospheric flank [e.g., *Miura, 1984; Saunders, 1990*]. The interaction is expected to be dawn-dusk symmetric at the magnetospheric boundary and hence to generate symmetric field-aligned currents. This is the scenario of the numerical model of *Rasmussen and Schunk [1987]* that we have just considered. The asymmetrical distribution of potential variation is a consequence of the ionospheric conductivity distribution but the total polar cap potential drop,  $\sim 19$  kV, is very nearly the expected sum. Thus the residual normal cells depicted in Figure 9 for strong  $B_z+$  are consistent with viscous cells modified by conductivity effects. In their event study, *Lu et al. [1994]* found viscous cells only on the duskside in the northern hemisphere. Our results suggest that there is a general asymmetry in the sizes of the viscous convection cells.

The reasons for a pronounced IMF effect on nightside con-

vection are not entirely clear. For example, the modeling work of *Moses et al. [1987]* generates the classical  $B_y$ -shaping of the dayside flow but predicts almost no nightside dependence. A reconnected flux tube on the dayside initially has an east-west motion that depends on the sign of  $B_y$ , but may be expected to turn poleward due to the antisunward magnetosheath flow. The effects of IMF on the nightside might then be felt only through the modulation of the overall size of the polar cap [*Lockwood et al., 1990*]. Moreover, the nightside convection responds to IMF conditions at the magnetopause at significant time delays. Coupled with variability in the IMF on comparable timescales and IMF dependencies in the rate of propagation of convection reconfiguration, such delays might be expected to greatly weaken any nightside IMF effect. Finally, substorm processes perturb the convection in the midnight sector in a manner thought to be largely independent of IMF-driven dayside merging.

Nevertheless, we have found that the  $B_y$  dependence extends into the nightside. Perhaps the reconnection on the nightside that completes the closed-open-closed field line cycle is influenced by the IMF content of the open field line. Alternatively, one could postulate the existence of an "inertial" aspect in the high-latitude convection such that flow deflected zonally on the dayside due to  $B_y$ -influenced reconnection retains the imprint of its initial deflection on its transit through the polar cap. As described by *Cowley et al. [1991]*, the asymmetrical transport of tubes of open flux into the crescent-shaped cell results in compressive forces; these may tend to relax in the higher polar cap by means of a compensatory drift across the pole. The result is an inclination of the flow contours in the polar cap with respect to the noon-midnight meridian that is opposite and more

gradual than that in the dayside reconnection region. The  $B_y$  effect then reaches into the nightside and closure of the deflected flow imparts curvature to the contours in the lower-latitude regions similar to that observed on the dayside.

The topological models of convection for northward IMF were reviewed by Crooker [1992] and the two basic modes were discussed by Greenwald *et al.* [1995a]. The merging points lie at points poleward of the cusp that are antiparallel to the geomagnetic field. In the case of lobe cell reconnection, the IMF merges with open polar cap field lines resulting in circulation of polar cap plasma. For dominant  $B_{z+}$  two cells are postulated while for  $B_{z+}$  but dominant  $B_y$  a single cell circulates on open field lines that fill the polar cap. In the second case, merging occurs sunward of the Earth in one hemisphere producing overdraped field lines that pass both sunward and tailward. The hemisphere favored for merging is that which presents its merging site first to the IMF as a result of dipole tilt and  $B_x$  factors. The open sunward field line may reconnect in the unfavored hemisphere resulting in a closed-open-closed field line cycle. In this mode polar cap merging produces reverse convection in both hemispheres. Alternatively, the internal reconnection site might not be active, leaving the unfavored hemisphere in a near-dormant condition and restricting sunward convection to the favored hemisphere.

As we have noted, our observations are primarily winter and equinoctial. If the polar cap merging model with merging restricted to the favored hemisphere were to apply, we would expect little evidence of reverse convection in the aggregate statistics. The fact that such circulation is obtained suggests that reverse convection is generally present for dominant  $B_{z+}$ , that is, the polar cap model with merging confined to one hemisphere, such as that observed in one case by Lu *et al.* [1994], is not statistically predominant.

This leaves the lobe cell model and the polar cap model with merging in both hemispheres. For lobe cell merging we would expect, with increase in  $B_y$  content, that a single dominant lobe cell in the polar cap would result. The polarity of the lobe cell would be set by the sign of  $B_y$ , westward across the noon meridian in the northern hemisphere for  $B_{y+}$  and eastward for  $B_{y-}$ . However, we have found little evidence of a dominant lobe cell for  $B_{y-}$ ; rather, the fundamental pattern is two-cell with domination by the dusk cell. Increasing the  $B_{z+}$  content imparts greater structure to the dusk cell dayside circulation and culminates in reverse convection cells. Elimination of the lobe cell model leaves polar cap merging in the favored hemisphere with reconnection active in both hemispheres as the statistically dominant scenario for  $B_{z+}$ . An event of this type was described by Greenwald *et al.* [1995a].

In the ongoing controversy regarding the number of convection cells expected for  $B_{z+}$ , we side with Clauer and Friis-Christensen [1988] in favoring distorted two-cell convection for nondominant  $B_{z+}$  and multicell for dominant  $B_{z+}$ . As the IMF becomes increasingly northward, a reverse convection cell may first appear on the prenoon side of the noon meridian resulting in a three-cell pattern of circulation; four-cell circulation is obtained when a weaker reverse convection cell then appears on the postnoon side. Progression of the convection from distorted two-cell to multicell for increasing  $B_{z+}$  content has been reported in case studies by Knipp *et al.* [1993], Lu *et al.* [1994], and Greenwald *et al.* [1995a]; our results and those of Weimer [1995] indicate that this progression is statistically prevalent.

## 6. Concluding Remarks

We have described the IMF dependencies of high-latitude convection derived from observations with the Goose Bay HF radar. These were summarized in graphical form in the plots of Figures 5–9. Several aspects of the dependencies are especially noteworthy. The IMF  $B_y$  component has a global effect on the predominant two-cell structure of convection. It can be characterized as shaping the cells into complementary round and crescent-shaped configurations and rotating the overall pattern in MLT. The  $B_y$  effect is seen on the nightside and possesses a hemispheric antisymmetry analogous to that on the dayside. For strongly northward IMF, reverse convection cells form on the dayside, and a multicell pattern is obtained.

Our findings are in many important respects consistent with those of the recent satellite studies. We believe that the agreement between these models establishes a standard for the evaluation of other statistical models. Our comparisons with the models that have been derived on the basis of magnetometer measurements [Friis-Christensen *et al.*, 1985; Papitashvili *et al.*, 1994] indicate a serious discrepancy in the basic size relationship of the two cells. The discrepancy may be a consequence of the conductivity models that have been used in the derivation of the magnetometer models. It may be interesting to combine the statistical measurements of electric fields from the radars and satellites with the equivalent currents implied by the magnetometer measurements to infer effective distributions of ionospheric conductivity.

We acknowledge that statistical patterns can not account for the full range of possible convection configurations. The event-to-event variability, even for selected IMF conditions, is usually quite pronounced. A statistical model is useful for defining a zero-order solution for the global convection that is keyed to a manageably small number of inputs. The extent to which the patterns are realized in the ionosphere can best be demonstrated by comparison with the results of large-scale mapping of the real-time convection. With the recent expansion of the SuperDARN system of HF radars, real-time high-resolution mapping of high-latitude convection is now possible through 12 hours of MLT in the northern hemisphere [Greenwald *et al.*, 1995b]. In a future paper we will report on comparisons of real-time SuperDARN mappings of convection with the results of statistical models. One match already noted here is the emergence of multicell convection for IMF strongly northward [Greenwald *et al.*, 1995a].

The patterns presented in this paper may be obtained from the authors in a variety of formats. The appendix lists the coefficients for the patterns of Figure 6, that is, for sorting by IMF angle in the GSM  $y$ - $z$  plane and  $2- \leq Kp \leq 3+$ .

## Appendix

Table A1 lists the sets of coefficients that specify the patterns of Figure 6. The potential is expanded in terms of spherical harmonics as described by Equations (9)–(12). Angle  $\alpha$  is the IMF angle in the GSM  $y$ - $z$  plane as defined in the text and  $\Lambda_0 = 60^\circ$ .

The coefficients indexed by negative values of  $m$ ,  $A_{l,-m}$ , can be obtained from the  $A_{lm}$  by applying the relations:

$$\operatorname{Re}(A_{l,-m}) = (-1)^m \operatorname{Re}(A_{lm}) \quad (\text{A1})$$

$$\operatorname{Im}(A_{l,-m}) = (-1)^{m+1} \operatorname{Im}(A_{lm}) \quad (\text{A2})$$

**Table A1.** Coefficients of the Spherical Expansions of the Potential Patterns of Figure 6

$l/m$	0	1	2	3	4	5	6
$\alpha = 0^\circ$							
0	-14.785	0.000					
1	-7.439	0.000	-0.903	11.898			
2	2.498	0.000	0.367	2.856	1.626	-2.509	
3	0.366	0.000	-0.084	-2.996	0.859	0.733	0.105 0.720
4	-0.580	0.000	0.282	-0.926	-0.459	-0.673	-0.195 -1.984 0.324 0.282
5	0.298	0.000	-0.124	0.900	0.189	-0.806	-0.242 -0.066 -0.008 -0.440 0.183 -0.011
6	-0.104	0.000	0.005	0.489	-0.132	0.349	-0.197 -0.360 0.229 -0.051 0.171 -0.335 0.150 -0.217
$\alpha = 45^\circ$							
0	14.959	0.000					
1	-12.445	0.000	-5.084	13.262			
2	-2.372	0.000	-2.220	6.207	2.156	-4.292	
3	0.897	0.000	-0.604	-3.283	-0.394	1.436	0.192 0.053
4	1.027	0.000	-0.496	-1.042	-1.750	-0.098	0.675 -1.486 -0.115 0.440
5	0.868	0.000	0.066	0.673	-0.051	-0.782	-0.418 -0.272 0.075 -0.821 -0.346 -0.031
6	-0.005	0.000	0.559	0.166	-0.070	0.118	-0.327 -0.311 0.036 0.620 0.185 -0.588 0.247 -0.086
$\alpha = 90^\circ$							
0	-15.827	0.000					
1	-15.084	0.000	-7.395	21.373			
2	-4.634	0.000	-4.295	9.986	2.235	-3.429	
3	1.202	0.000	-0.670	-2.818	-1.394	3.529	0.481 0.257
4	2.203	0.000	-0.392	-1.261	-2.480	0.229	0.432 -0.280 -0.024 -0.023
5	1.070	0.000	0.200	0.539	0.481	-0.389	-0.438 0.110 -0.114 0.001 -0.257 -0.199
6	-0.411	0.000	0.645	-0.118	0.306	-0.077	-0.298 -0.154 -0.184 0.399 -0.019 -0.315 0.189 0.173
$\alpha = 135^\circ$							
0	-23.288	0.000					
1	-15.606	0.000	-13.931	28.009			
2	-0.656	0.000	-5.386	10.115	3.815	-3.495	
3	1.621	0.000	-0.002	-4.084	-1.732	4.413	1.115 -0.144
4	1.802	0.000	0.617	-1.760	-1.549	-0.394	-0.078 0.888 0.297 -0.300
5	0.084	0.000	0.448	0.793	0.648	-0.587	-0.126 -0.134 -0.450 0.272 0.009 -0.477
6	-0.978	0.000	0.554	0.098	0.359	-0.091	-0.296 0.146 -0.309 -0.020 0.087 0.014 0.317 0.103
$\alpha = 180^\circ$							
0	-24.434	0.000					
1	-9.216	0.000	-16.200	36.590			
2	3.832	0.000	-2.469	7.863	1.832	-1.908	
3	-1.283	0.000	1.191	-4.745	-1.327	4.234	0.293 -1.213
4	0.660	0.000	0.955	-1.726	0.174	-0.930	-0.681 0.482 0.262 -0.125
5	0.277	0.000	-0.624	1.101	0.292	-0.554	0.291 -0.358 -0.638 -0.022 0.415 0.162
6	-0.660	0.000	0.072	0.317	-0.148	-0.067	0.062 0.486 0.452 -0.276 -0.127 0.042 -0.343 0.208
$\alpha = 225^\circ$							
0	-17.722	0.000					
1	-2.596	0.000	-10.192	33.209			
2	6.841	0.000	-0.437	7.566	-0.578	-2.463	
3	-2.073	0.000	1.286	-2.936	0.677	2.143	-0.546 0.591
4	-1.564	0.000	0.681	-1.117	0.694	0.015	-0.713 -0.289 -0.193 0.354
5	0.250	0.000	-0.699	0.360	0.381	-0.151	-0.273 0.009 -0.360 -0.145 0.436 0.532
6	0.149	0.000	-0.074	-0.197	-0.423	0.031	0.222 0.359 -0.111 0.141 0.014 -0.150 0.134 0.100
$\alpha = 270^\circ$							
0	-13.126	0.000					
1	-1.075	0.000	-4.436	28.058			
2	7.221	0.000	-0.027	7.546	-0.461	-3.331	
3	-0.842	0.000	1.343	-2.119	0.711	1.576	-0.643 0.569
4	-2.285	0.000	0.914	-0.852	0.060	0.043	-0.683 -0.332 -0.745 0.009
5	-0.105	0.000	-0.508	0.238	0.649	-0.196	-0.138 -0.316 -0.008 -0.022 0.322 0.141
6	0.123	0.000	-0.234	-0.186	0.006	0.205	0.070 -0.013 0.002 -0.031 0.212 -0.028 0.094 0.141
$\alpha = 315^\circ$							
0	-15.113	0.000					
1	-3.574	0.000	-2.877	21.421			
2	6.648	0.000	0.421	5.965	-0.234	-3.029	
3	-0.044	0.000	0.824	-2.024	1.304	1.422	-0.353 1.104
4	-2.059	0.000	1.012	-0.786	-0.458	-0.118	-0.735 -0.503 0.081 0.099
5	-0.161	0.000	-0.201	0.418	0.656	-0.401	-0.071 0.101 -0.287 -0.460 0.410 0.240
6	-0.005	0.000	-0.267	-0.049	0.103	0.266	0.081 -0.249 0.209 0.085 0.146 -0.146 -0.029 0.238

**Acknowledgments.** This work was supported by the National Science Foundation (NSF) Division of Aeronomy under NSF grants ATM-9102316 and ATM-9416310. The Johns Hopkins University Applied Physics Laboratory HF radar at Goose Bay, Labrador, is supported by the NSF Division of Atmospheric Sciences under NSF grant ATM-9502993 and by the National Aeronautics and Space Administration (NASA) under NASA grant NAG5-1099. The authors thank B. Gill for his assistance in the day-to-day operation of the radar and the Ionospheric Effects Branch of the Phillips Laboratory for support in operating from the Goose Bay field site. They also thank J. King and N. Papitashvili for their assistance in providing IMP8 magnetometer data.

The editor thanks F. J. Rich and T. J. Rosenberg for their assistance in evaluating this paper.

## References

- Alcaydé, D., G. Caudal, and J. Fontanari, Convection electric fields and electrostatic potential over  $61^\circ < \Lambda < 72^\circ$  invariant latitude observed with the European incoherent scatter facility, 1, Initial results, *J. Geophys. Res.*, **91**, 233–247, 1986.
- Atkinson, G., and D. Hutchison, Effect of the day night ionospheric conductivity gradient on polar cap convective flow, *J. Geophys. Res.*, **83**, 725–729, 1978.
- Axford, W. I., and C. O. Hines, A unifying theory of high latitude geophysical phenomena and geomagnetic storms, *Can. J. Phys.*, **69**, 1181, 1961.
- Baker, K. B., R. A. Greenwald, J. P. Villain, and S. Wing, Spectral characteristics of high frequency (HF) backscatter for high latitude ionospheric irregularities: Preliminary analysis of statistical properties, *Tech. Rep. RADC-TR-87-284*, Rome Air Dev. Cent., Griffis Air Force Base, N. Y., 1988.
- Baker, K. B., and S. Wing, A new magnetic coordinate system for conjugate studies of high latitudes, *J. Geophys. Res.*, **94**, 9139–9143, 1989.
- Bargatze, L. F., D. N. Baker, R. L. McPherron, and E. W. Hones Jr., Magnetic impulse response to many levels of geomagnetic activity, *J. Geophys. Res.*, **90**, 6387–6393, 1985.
- Berthelier, A., J. J. Bethelier, and C. Guerin, The effect of the east-west component of the interplanetary magnetic field on magnetospheric convection as deduced from magnetic perturbations at high latitudes, *J. Geophys. Res.*, **79**, 3187–3192, 1974.
- Burch, J. L., P. H. Reiff, J. D. Menietti, R. A. Heelis, W. B. Hanson, S. D. Shawhan, E. G. Shelley, M. Sugiura, D. R. Weimer, and J. D. Winningham, IMF  $B_y$ -dependent plasma flow and Birkeland currents in the dayside magnetosphere, 1, Dynamics explorer observations, *J. Geophys. Res.*, **90**, 1577–1593, 1985.
- Clauer, C. R., and E. Friis-Christensen, High-latitude dayside electric fields and currents during strong northward interplanetary magnetic field: Observations and simulation, *J. Geophys. Res.*, **93**, 2749–2757, 1988.
- Cowley, S. W. H., J. P. Morelli, and M. Lockwood, Dependence of convective flows and particle precipitation in the high-latitude dayside ionosphere on the X and Y components of the interplanetary magnetic field, *J. Geophys. Res.*, **96**, 5557–5564, 1991.
- Crooker, N. U., and F. J. Rich, Lobe cell convection as a summer phenomenon, *J. Geophys. Res.*, **98**, 13,403–13,407, 1993.
- Crooker, N. U., Reverse convection, *J. Geophys. Res.*, **97**, 19,363–19,372, 1992.
- Crooker, N. U., Dayside merging and cusp geometry, *J. Geophys. Res.*, **84**, 951–959, 1979.
- de la Beaujardière, O., D. Alcaydé, J. Fontanari, and C. Leger, Seasonal dependence of high-latitude electric fields, *J. Geophys. Res.*, **96**, 5723–5735, 1991.
- de la Beaujardière, O., V. B. Wickwar, J. D. Kelly, and J. H. King, Effect of the interplanetary magnetic field y component on the high-latitude nightside convection, *Geophys. Res. Lett.*, **12**, 461–464, 1985.
- de la Beaujardière, O., V. B. Wickwar, and J. H. King, Sondrestrom radar observations of the effect of the IMF  $B_y$  component on polar cap convection, in *Solar Wind-Magnetosphere Coupling*, edited by Y. Kamide and J. A. Slavin, pp. 495–505, D. Reidel, Norwell, Mass., 1986.
- Dudeney, J. R., A. S. Rodger, M. Pinnock, J. M. Ruohoniemi, K. B. Baker, and R. A. Greenwald, Studies of conjugate plasma convection in the vicinity of the Harang discontinuity, *J. Atmos. Terr. Phys.*, **53**, 249–263, 1991.
- Dungey, J. W., Interplanetary magnetic fields and the auroral zones, *Phys. Rev. Lett.*, **6**, 47–48, 1961.
- Dungey, J. W., The structure of the exosphere, or adventures in velocity space, in *Geophysics: The Earth's Environment*, edited by C. DeWitt, J. Hieblot, and A. Lebeau, pp. 503–550, Gordon and Breach, New York, 1963.
- Foster, J. C., An empirical electric field model derived from Chatanika radar data, *J. Geophys. Res.*, **88**, 981–987, 1983.
- Foster, J. C., J. M. Holt, and R. G. Musgrove, Ionospheric convection associated with discrete levels of particle precipitation, *Geophys. Res. Lett.*, **13**, 1986a.
- Foster, J. C., J. M. Holt, R. G. Musgrove, and D. S. Evans, Solar wind dependencies of high-latitude convection and precipitation, in *Solar Wind-Magnetosphere Coupling*, edited by Y. Kamide and J. A. Slavin, pp. 477–494, D. Reidel, Norwell, Mass., 1986b.
- Freeman, M. P., and D. J. Southwood, The effect of magnetospheric erosion on mid- and high-latitude ionospheric flows, *Planet. Space Sci.*, **36**, 509–522, 1988.
- Freeman, M. P., J. M. Ruohoniemi, and R. A. Greenwald, The determination of time-stationary two-dimensional convection patterns with single-station radars, *J. Geophys. Res.*, **96**, 15,735–15,749, 1991.
- Friis-Christensen, E., Y. Kamide, A. D. Richmond, and S. Matsushita, Interplanetary magnetic field control of high-latitude electric fields and currents determined from Greenland magnetometer data, *J. Geophys. Res.*, **90**, 1325–1338, 1985.
- Greenwald, R. A., K. B. Baker, R. A. Hutchins, and C. Hanuise, An HF phased-array radar for studying small-scale structure in the high-latitude ionosphere, *Radio Sci.*, **20**, 63, 1985.
- Greenwald, R. A., K. B. Baker, J. M. Ruohoniemi, J. R. Dudeney, M. Pinnock, N. Mattin, J. M. Leonard, and R. P. Lepping, Simultaneous conjugate observations of dynamic variations in high-latitude dayside convection due to changes in IMF  $B_y$ , *J. Geophys. Res.*, **95**, 8057–8072, 1990.
- Greenwald, R. A., W. A. Bristow, G. J. Sofko, C. Senior, J.-C. Cerisier, and A. Szabo, Super Dual Auroral Radar Network radar imaging of dayside high-latitude convection under northward interplanetary magnetic field: Toward resolving the distorted two-cell versus multicell controversy, *J. Geophys. Res.*, **100**, 19,661–19,674, 1995a.
- Greenwald, R. A., et al., DARN/SuperDARN: A global view of high-latitude convection, *Space Sci. Rev.*, **71**, 763–796, 1995b.
- Heelis, R. A., The effects of interplanetary orientation on dayside high-latitude convection, *J. Geophys. Res.*, **89**, 2873–2880, 1984.
- Hepner, J. P., Polar cap electric field distributions related to interplanetary magnetic field direction, *J. Geophys. Res.*, **77**, 4877, 1972.

- Heppner, J. P., and N. C. Maynard, Empirical high-latitude electric field models, *J. Geophys. Res.*, **92**, 4467–4489, 1987.
- Holt, J. M., R. H. Wand, J. V. Evans, and W. L. Oliver, Empirical models for the plasma convection at high latitudes from Millstone Hill observations, *J. Geophys. Res.*, **92**, 203–212, 1987.
- Holzworth, R. H., and C.-I. Meng, Auroral boundary variations and the interplanetary magnetic field, *Planet. Space Sci.*, **32**, 25, 1984.
- Iijima, T., T. A. Potemra, L. J. Zanetti, and P. F. Bythrow, Large-scale Birkeland currents in the dayside polar region during strongly northward IMF, *J. Geophys. Res.*, **89**, 7441–7452, 1984.
- Iijima, T., and T. A. Potemra, Large-scale characteristics of field-aligned currents associated with substorms, *J. Geophys. Res.*, **83**, 599–615, 1978.
- Jackson, J. D., *Classical Electrodynamics*, John Wiley, New York, 1962.
- Jones, T. B., Radar studies of high-latitude ionospheric flows, *Philos. Trans. R. Soc. London, Ser. A*, **328**, 107–118, 1989.
- Kamide, Y., W. Sun, and S.-I. Akasofu, The average ionospheric electrodynamics for the different substorm phases, *J. Geophys. Res.*, **101**, 99–109, 1996.
- Knipp, D. J., et al., Ionospheric convection response to slow, strong variations in a northward interplanetary magnetic field: A case study for 14 January 1988, *J. Geophys. Res.*, **98**, 19,273–19,292, 1993.
- Leonard, J. M., The phenology of Antarctic *F*-region irregularities, M. S. thesis, The Brit. Antarctic Surv., Cambridge, England, 1991.
- Leonard, J. M., M. Pinnock, A. S. Rodger, J. R. Dudeney, R. A. Greenwald, and K. B. Baker, Ionospheric plasma convection in the southern hemisphere, *J. Atmos. Terr. Phys.*, **57**, 889–897, 1995.
- Lockwood, M., S. W. H. Cowley, and M. P. Freeman, The excitation of plasma convection in the high latitude ionosphere, *J. Geophys. Res.*, **95**, 7961–7972, 1990.
- Lu, G., et al., Interhemispheric asymmetry of the high-latitude ionospheric convection pattern, *J. Geophys. Res.*, **99**, 6491–6510, 1994.
- Maynard, N. C., and J. P. Heppner, Variations in electric fields from polar orbiting satellites, in *Particles and Fields in the Magnetosphere*, edited by B. M. McCormac, pp. 247–253, D. Reidel, Norwell, Mass., 1970.
- Maynard, N. C., W. F. Denig, and W. J. Burke, Mapping ionospheric convection patterns to the magnetosphere, *J. Geophys. Res.*, **100**, 1713–1721, 1995.
- Miura, A., Anomalous transport by magnetohydrodynamic Kelvin-Helmholtz instabilities in the solar wind-magnetosphere interaction, *J. Geophys. Res.*, **89**, 801–818, 1984.
- Moses, J. J., G. L. Siscoe, N. U. Crooker, and D. J. Gorney, IMF *B<sub>y</sub>* and day-night conductivity effects in the expanding polar cap convection model, *J. Geophys. Res.*, **92**, 1193–1198, 1987.
- Papitashvili, V. O., B. A. Belov, D. S. Faermark, Y. I. Feldstein, S. A. Golyshev, L. I. Gromova, and A. E. Levitin, Electric potential patterns in the northern and southern polar regions parameterized by the interplanetary magnetic field, *J. Geophys. Res.*, **99**, 13,251–13,262, 1994.
- Papitashvili, V. O., C. R. Clauer, A. E. Levitin, and B. A. Belov, Relationship between the observed and modeled modulation of the dayside ionospheric convection by the IMF *B<sub>y</sub>* component, *J. Geophys. Res.*, **100**, 7715–7722, 1995.
- Rasmussen, C. E., and R. W. Schunk, Ionospheric convection driven by NBZ currents, *J. Geophys. Res.*, **92**, 4491–4504, 1987.
- Reiff, P. H., and J. L. Burch, IMF *B<sub>y</sub>*-dependent plasma flow and Birkeland currents in the dayside magnetosphere, 2, A global model for northward and southward IMF, *J. Geophys. Res.*, **90**, 1595–1609, 1985.
- Reiff, P. H., and R. A. Heelis, Four cells or two? Are four convection cells really necessary?, *J. Geophys. Res.*, **99**, 3955–3959, 1994.
- Rich, F. J., and M. Hairston, Large-scale convection patterns observed by DMSP, *J. Geophys. Res.*, **99**, 3827–3844, 1994.
- Ruohoniemi, J. M., and R. A. Greenwald, Observations of IMF and seasonal effects in high-latitude convection, *Geophys. Res. Lett.*, **9**, 1121–1124, 1995.
- Ruohoniemi, J. M., R. A. Greenwald, K. B. Baker, J. P. Villain, and M. A. McCready, Drift motions of small-scale irregularities in the high-latitude *F* region: An experimental comparison with plasma drift motions, *J. Geophys. Res.*, **92**, 4553–4564, 1987.
- Ruohoniemi, J. M., R. A. Greenwald, O. de la Beaujardière, and M. Lester, The response of the high-latitude dayside ionosphere to an abrupt northward transition in the IMF, *Ann. Geophys.*, **11**, 544–555, 1993.
- Russell, C. T., The configuration of the magnetosphere, in *Critical Problems of Magnetospheric Physics*, edited by E. R. Dyer, pp. 1–16, Inter-Union Comm. on Solar Terr. Phys. Sec., Natl. Acad. of Sci., Washington, D. C., 1972.
- Saunders, M. A., Magnetosheath, magnetopause, and low latitude boundary layer research, 1987–1989, *J. Atmos. Terr. Phys.*, **52**, 1107, 1990.
- Scourfield, M. W. J., and E. Nielsen, Evening (Harang) and morning discontinuities in ionospheric electron drifts and their dependence on the interplanetary magnetic field, *J. Geophys. Res.*, **86**, 681–686, 1981.
- Senior, C., D. Fontaine, G. Caudal, D. Alcaydé, and J. Fontanari, Convection electric fields and electrostatic potential over  $61^\circ < \Lambda < 72^\circ$  invariant latitude observed with the European incoherent scatter facility, 2, Statistical results, *Ann. Geophys.*, **8**, 257–272, 1990.
- Shue, J.-H., and D. R. Weimer, The relationship between ionospheric convection and magnetic activity, *J. Geophys. Res.*, **99**, 401–415, 1994.
- Villain, J. P., G. Caudal, and C. Hanuise, A SAFARI-EISCAT comparison between the velocity of *F* region small-scale irregularities and the ion drift, *J. Geophys. Res.*, **90**, 8433, 1985.
- Waldock, J. A., T. B. Jones, and E. Nielsen, Mean auroral *E*-region plasma convection patterns measured by SABRE, *Nature*, **313**, 204–206, 1985.
- Wand, R. H., and J. V. Evans, The penetration of convection electric fields to the latitude of Millstone Hill ( $\Lambda = 56^\circ$ ), *J. Geophys. Res.*, **86**, 5809–5814, 1981.
- Weimer, D. R., Models of high-latitude electric potentials derived with a least error fit of spherical harmonic coefficients, *J. Geophys. Res.*, **100**, 19,595–19,607, 1995.

---

J. M. Ruohoniemi and R. A. Greenwald, The Johns Hopkins University Applied Physics Laboratory, Johns Hopkins Road, Laurel, MD 20723-6099. (e-mail: mike\_ruohoniemi@jhuapl.edu; ray\_greenwald@jhuapl.edu)

(Received March 8, 1996; revised May 14, 1996; accepted May 17, 1996.)